INFALL, OUTFLOW, ROTATION, AND TURBULENT MOTIONS OF DENSE GAS WITHIN NGC 1333 IRAS 4

JAMES DI FRANCESCO,[1] PHILIP C. MYERS, DAVID J. WILNER, NAGAYOSHI OHASHI,[2] AND DIEGO MARDONES[3]

Harvard-Smithsonian Center for Astrophysics, 60 Garden Street, MS 42, Cambridge, MA 02138

ABSTRACT

Millimeter wavelength observations are presented of NGC 1333 IRAS 4, a group of highly embedded young stellar objects in Perseus, that reveal motions of infall, outflow, rotation, and turbulence in the dense gas around its two brightest continuum objects, 4A and 4B. These data have finest angular resolution of $\sim 2''$ (0.0034 pc) and finest velocity resolution of 0.13 km s^{-1}. Infall motions are seen from inverse P Cygni profiles observed in H_2CO 3_{12}–2_{11} toward both objects, but also in CS 3–2 and N_2H^+ 1–0 toward 4A, providing the least ambiguous evidence for such motions toward low-mass protostellar objects. Outflow motions are probed by bright line wings of H_2CO 3_{12}–2_{11} and CS 3–2 observed at positions offset from 4A and 4B, likely tracing dense cavity walls. Rotational motions of dense gas are traced by a systematic variation of the N_2H^+ line velocities, and such variations are found around 4A but not around 4B. Turbulent motions appear reduced with scale, given N_2H^+ line widths around both 4A and 4B that are narrower by factors of 2 or 3 than those seen from single-dish observations. Minimum observed line widths of ~ 0.2 km s^{-1} provide a new low, upper bound to the velocity dispersion of the parent core to IRAS 4 and demonstrate that turbulence within regions of clustered star formation can be reduced significantly. A third continuum object in the region, 4B', shows no detectable line emission in any of the observed molecular species.

Subject headings: ISM: individual (NGC 1333 IRAS 4) — ISM: kinematics and dynamics — ISM: molecules — stars: formation — stars: pre–main-sequence

1. INTRODUCTION

Star formation involves both coherent and incoherent gas motions within molecular clouds. Coherent motions are those with an implicitly common directionality and include the infall, outflow, and rotational motions of molecular gas associated with extremely young protostellar objects (Mardones et al. 1997, hereafter M97); Gregersen et al. 1997; Bontemps et al. 1996; Ohashi et al. 1997). Incoherent motions have no directionality, appear random, and include thermal motions within molecular gas and nonthermal motions of turbulence (i.e., randomly propagating MHD waves; Arons & Max 1975).

Understanding gas motions is crucial to understanding the overall flow of mass during the star formation process, and this is typically attempted by analyzing molecular gas line profiles. In practice, however, different types of motion can be difficult to distinguish because similar line profiles can be produced when different molecular gas motions are projected along the line of sight. For example, asymmetrically blue optically thick lines relative to symmetric optically thin lines have been interpreted recently as evidence for infall motions in several molecular cloud cores (e.g., see Leung & Brown 1977; Zhou et al. 1993). However, outflow or rotational motions of molecular gas can also produce such a signature, especially at velocities that are low relative to the systemic velocity (see Adelson & Leung

1988; Cabrit & Bertout 1986). In addition, thermal and nonthermal motions each act to broaden line widths and together can potentially obscure signatures of other motions.

Analysis of the gas motions associated with star formation is further complicated by the fact that stars form in groups. For example, young stars are found by number more in close proximity within massive, turbulent cloud cores (as in Orion, Perseus, or Ophiuchus) than in isolation in less massive, nonturbulent cores (as in Taurus or Lupus; see Lada, Strom, & Myers 1993). Given the finite resolutions of millimeter telescopes, the apparent proximity on the sky of several protostellar objects within a group can confuse the relationships between observed molecular gas motions and individual objects, especially in more distant regions.

Millimeter interferometers can minimize the problems of ascribing various types of motion to gas within regions where groups of young stellar objects are forming, by providing high-resolution observations of judiciously chosen molecular lines. For example, lines observed at high resolution can yield profiles that are less ambiguous in interpretation. Furthermore, the high resolution can allow a better determination of the spatial association of gas with specific objects in a crowded field. In addition, high-resolution observations can reveal strikingly the abundance contrasts between outflowing and nonoutflowing gas, so observing species particularly abundant in either of these components can better trace its specific motions.

In this paper we present millimeter interferometer observations of the NGC 1333 IRAS 4 region in the L1430 core of Perseus to probe the individual coherent and incoherent motions associated with a small group of protostellar objects. NGC 1333 itself is a region forming many proto-

[1] Current address: Radio Astronomy Laboratory, 601 Campbell Hall, University of California, Berkeley, Berkeley, CA 94720-3411.

[2] Current address: Institute of Astronomy and Astrophysics, Academia Sinica, P.O. Box 1-87, Nankang, Taipei 11529, Taiwan.

[3] Current address: Departamento de Astronomía, Universidad de Chile, Casilla 36-D, Santiago, Chile.

stellar groups and has a 350 pc distance[4] (Herbig & Jones 1983).

IRAS 4 consists of four (or more) very embedded objects located within a 30″ (0.05 pc) radius, all ∼3′ (0.3 pc) southeast of SVS 13. IRAS 4 was discovered by Jennings et al. (1987) as a single IRAS source and later resolved by Sandell et al. (1991) into 4A and 4B, separated by 30″. Although 4A and 4B together were considered one of the first "protobinaries" ever detected (see Mathieu 1994), each object is itself multiple. IRAS 4A was resolved into 4A and 4A′, with 2″ separation, by Lay, Carlstrom, & Hills (1995), and IRAS 4B was resolved into two objects, 4B and 4B′, with 10″ separation, by Looney, Mundy, & Welch (2000). The 4B object itself also may be a binary or triple system of less than 0″.5 separation, although this remains unconfirmed. The 4B′ object has been named differently by other groups who detected it contemporaneously, i.e., 4BII by Smith et al. (2000), 4BE by Sandell & Knee (2001), and 4C by Looney et al. (2000) and Choi, Panis, & Evans (1999). We name the object 10″ east of 4B as 4B′ because 4C was used by Rodríguez, Anglada, & Curiel (1999) and Sandell & Knee (2001) to name a millimeter object ∼40″ east by northeast of 4A. The spectral energy distributions (SEDs) of 4A and 4B are both very red, suggesting that IRAS 4 consists of several "Class 0" objects, each at the earliest observed stage of protostellar evolution (i.e., $t \approx 10^4$ yr or less; see André, Ward-Thompson, & Barsony 1993).

IRAS 4 has been identified previously as a site of outflow and possibly infall in a turbulent region forming clusters. Using single-dish observations of numerous millimeter and submillimeter emission lines, Blake et al. (1995, hereafter B95) probed abundance depletions and enhancements in the gas associated with 4A or 4B. Low-velocity line emission (i.e., at $\Delta V \approx 1$–2 km s^{-1} relative to the systemic velocity) revealed a nonoutflowing gas component around each source, with abundance depletions by factors of 10–20 (relative to dust) due to the adsorption of molecules onto grains at the high densities ($n = 2 \times 10^6$ cm^{-3}) and low temperatures ($T_k = 20$–40 K) of the gas surrounding each object. The profiles of some optically thick lines seen by B95 were asymmetrically blue, suggesting that these gas components were infalling. Outflowing gas around each source was also detected from line wings seen at higher relative velocities. Qualitative differences in the outflows were found between sources, e.g., the 4A outflow extended 4′ tip to tip in CO and 1′ tip to tip in CS, but the 4B outflow extended only less than 20″ in either tracer. Despite these differences, however, abundance enhancements (relative to CO) were found in both outflows for several molecules including H$_2$CO, CS, and CH$_3$CO, likely as a result of the return of grain mantles to the gas phase from grain-grain collisions within outflow shear zones.

Further evidence for infall motions at 4A and 4B was obtained from the asymmetrically blue profiles of H$_2$CO 2_{12}–1_{11} and CS 2–1 by M97 and HCO$^+$ 4–3 and HCO$^+$ 3–2 by Gregersen et al. (1997). Mardones (1998, hereafter M98) further mapped IRAS 4 in H$_2$CO 2_{12}–1_{11} and H$_2$CO 3_{12}–2_{11} and found asymmetrically blue profiles throughout the region, but the most extreme self-absorptions were found at the positions of 4A and 4B (see also Mardones et al. 2001). Choi et al. (1999) mapped IRAS 4 in HCO$^+$ 1–0

and HCN 1–0 and again found asymmetrically blue emission profiles at the positions of each protostellar object. In addition, small redshifted absorption dips were seen in their HCN spectrum toward 4A, arising from infalling gas along the line of sight.

We describe our millimeter interferometer observations in § 2. A description of the H$_2$CO 3_{12}–2_{11}, CS 3–2, and N$_2$H$^+$ 1–0 data is presented in § 3. Discussion of the infall and outflow motions revealed by H$_2$CO and the rotational and turbulent motions revealed by N$_2$H$^+$ follows in § 4. In § 5 a concluding summary is presented. The Appendix describes the continuum data and the relative millimeter SEDs of 4A, 4B, and 4B′.

2. OBSERVATIONS

IRAS 4 was observed between 1997 July and 1998 March at the IRAM[5] Plateau de Bure Interferometer (PdBI), NRO[6] Nobeyama Millimeter Array (NMA), and the NRAO[7] Very Large Array (VLA). Table 1 lists the wavelengths, frequencies, configurations, and dates of observations made with each array, as well as the synthesized beam FWHM and the 1 σ (rms) continuum sensitivities obtained from combining all respective tracks.

2.1. Primary Observations

2.1.1. PdBI Data

At the IRAM PdBI, H$_2$CO 3_{12}–2_{11} at 225.7 GHz was observed to trace infall or outflow motions in the region, following M97 or B95 but using other H$_2$CO transitions and at higher resolution. Dense gas can be traced by this line, as its critical density $n_{cr} \approx 4.5 \times 10^6$ cm^{-3} (from Green 1991), but H$_2$CO may be depleted in dense gas surrounding protostellar objects and enhanced in outflows (see B95). In addition, N$_2$H$^+$ 1–0 at 93.17 GHz was observed to trace nonoutflowing dense gas in IRAS 4, following M97 but at higher resolution. This line is abundant in star-forming regions (e.g., Womack, Ziurys, & Wyckoff 1992) and has also a high critical density, i.e., $n_{cr} \approx 2 \times 10^5$ cm^{-3}. Furthermore, N$_2$H$^+$ is observed and predicted to remain relatively abundant in dense cores with $n \approx 10^4$–10^5 cm^{-3} (Benson, Caselli, & Myers 1998; Bergin & Langer 1997) but is possibly depleted, rather than enhanced, by outflow chemistry (see Bergin, Neufeld, & Melnick 1998). Continuum emission at $\lambda = 3.2$ and 1.3 mm was observed to locate each protostellar object in IRAS 4 from associated warm dust.

The 1 and 3 mm bands were observed simultaneously. Receiver 2 was tuned to observe H$_2$CO 3_{12}–2_{11} over 230 channels in a 20 MHz wide band, yielding a channel spacing of 0.10 km s^{-1} or a velocity resolution of 0.13 km s^{-1}. The remaining two correlator units were assigned to observe continuum emission at $\lambda = 1.3$ mm over a 300 MHz wide band. Receiver 1 was tuned to observe N$_2$H$^+$ 1–0 over 230 channels in a 10 MHz wide band, allowing all

TABLE 1

LOG OF OBSERVATIONS

λ (mm)	ν (GHz)	Interferometer	Configuration	Observing Dates	Beam FWHM (arcsec)	Continuum rms (mJy beam^{-1})
1.3	225.7	IRAM PdBI	5C2-W09	1997 Jul 21	2.0×1.7	17.5
			4ant-special	1997 Aug 19		
			5D-N09	1997 Sep 19		
			4D2+N13	1997 Nov 14		
2.0	147.0	NMA	D	1997 Dec 27	3.2×2.3^a	14.0
			C	1998 Mar 09		
2.2	137.0	NMA	D	1997 Dec 27	3.4×2.6	10.5
			C	1998 Mar 09		
3.2	93.2	IRAM PdBI	5C2-W09	1997 Jul 20	2.9×2.6	4.5
			5C2-W09	1997 Jul 21		
			4ant-special	1997 Aug 19		
			5D-N09	1997 Sep 19		
			4D2+N13	1997 Nov 14		
6.9	43.3	VLA	D	1997 Nov 25	2.1×1.9	0.30
13.3	22.5	VLA	D	1997 Nov 25	3.8×3.1	0.28

^{a} CS 3–2 data tapered to a $6.''5 \times 4.''4$ FWHM beam for Fig. 1e and analysis.

seven of its hyperfine components to be sampled with a channel spacing of 0.13 km s^{-1}, or a velocity resolution of 0.16 km s^{-1}. The other two correlator units were combined to observe continuum emission at $\lambda = 3.2$ mm in a 300 MHz wide band.

Each track with the IRAM PdBI consisted of three pointings centered on 4A, 4B, and a position halfway in between, interleaved with observations of 0415+379 (3C 111) or 0316+413 (3C 84) for phase and flux calibration. (The sources 2230+114 and MWC 349 were also observed as secondary flux calibrators.) With primary beam FWHM of $\sim 54''$ and $\sim 22''$ at 93.17 and 225.7 GHz, respectively, this pointing strategy allowed the construction of an over-sampled mosaic at $\lambda = 3.2$ mm and an undersampled mosaic at $\lambda = 1.3$ mm. Each track was calibrated in Grenoble, France using the IRAM software package CLIC. Data from each pointing were combined in the visibility plane and inverted simultaneously, and the resulting mosaics cleaned using the IRAM software package MAPPING. Further analysis was carried out using the MIRIAD, CLASS, and AIPS software packages.

2.2. Secondary Observations

2.2.1. NRO NMA Data

The CS 3–2 line at 146.97 GHz was observed at the NRO NMA in order to trace dense gas, as its $n_{cr} \approx 1.3 \times 10^6$ cm^{-3} (Evans 1999). Continuum emission at $\lambda = 2.2$ and 2.0 mm was observed in order to trace warm dust, improving the SED of each source.

The NMA FX correlator was tuned to observe CS 3–2 at 146.97 GHz, over 1024 channels in a 32 MHz wide band, for a channel spacing and velocity resolution of 0.064 km s^{-1}. The NMA Ultra-Wide Bandwidth Correlator was tuned over a 1024 MHz wide band to observe simultaneously continuum emission at $\lambda = 2.2$ and 2.0 mm in the lower and upper sidebands, respectively.

Each track with the NRO NMA consisted of two pointings centered on 4A and 4B, interleaved with observations of 0316+413 (3C 84) for phase and flux calibration. With a primary beam at 146.97 GHz of $\sim 51''$, this pointing strategy resulted in slightly undersampled mosaics at $\lambda = 2.2$ and 2.0 mm. Data from each track were calibrated in Nobeyama, Japan, using the software package UVPROC2.

Further analysis was carried out using the MIRIAD software packages. For better sensitivity of CS 3–2, the NMA data were tapered with a $4'' \times 4''$ FWHM Gaussian to obtain a final $6.''5 \times 4.''4$ FWHM synthesized beam.

2.2.2. NRAO VLA Data

Continuum emission at $\lambda = 6.9$ mm and 1.3 cm was observed with the NRAO VLA to trace dust, extending the SED of each source across the entire millimeter wavelength range. Observations at these wavelengths are also important because they set effective limits on the amounts of free-free emission within the SEDs of young stellar objects at shorter millimeter wavelengths, allowing the amounts of thermal emission solely from dust to be characterized more accurately (e.g., see Di Francesco et al. 1997).

Both bands were observed simultaneously by dividing the VLA into two subarrays, with 13 antennas observing at $\lambda = 6.9$ mm (43.34 GHz) using Q-band receivers and 14 antennas observing at $\lambda = 1.3$ cm (22.46 GHz) using K-band receivers, each over 100 MHz wide bands.

The NRAO VLA was pointed at one position halfway between 4A and 4B to include 4A, 4B, and 4B' within the $\sim 62''$ and $\sim 120''$ primary beam FWHM of the VLA antennas at $\lambda = 6.9$ mm and 1.3 cm, respectively. Observations of IRAS 4 were interleaved with observations of 0316+413 (3C 84) for phase calibration approximately every 10 minutes and X-band reference pointing checks approximately every 60 minutes. Observations of 0134+329 (3C 48) and 1328+307 (3C 286) were made for flux calibration at both wavelengths. Data from this track were calibrated in Socorro, New Mexico and further analyzed using the software package AIPS.

3. RESULTS

Figure 1 shows maps of IRAS 4 in continuum emission at $\lambda = 1.3$, 2.0, and 3.2 mm, as well as maps of the integrated intensities of the H_2CO 3_{12}–2_{11}, CS 3–2, and N_2H^+ 1–0 line emission (i.e., the "zeroth moment" obtained at a given position by summing emission from all channels except those containing values less than 2 σ).

3.1. Continuum

Figures 1a, 1b, and 1c illustrate the relative positions (in projection) of protostellar continuum objects in IRAS 4,
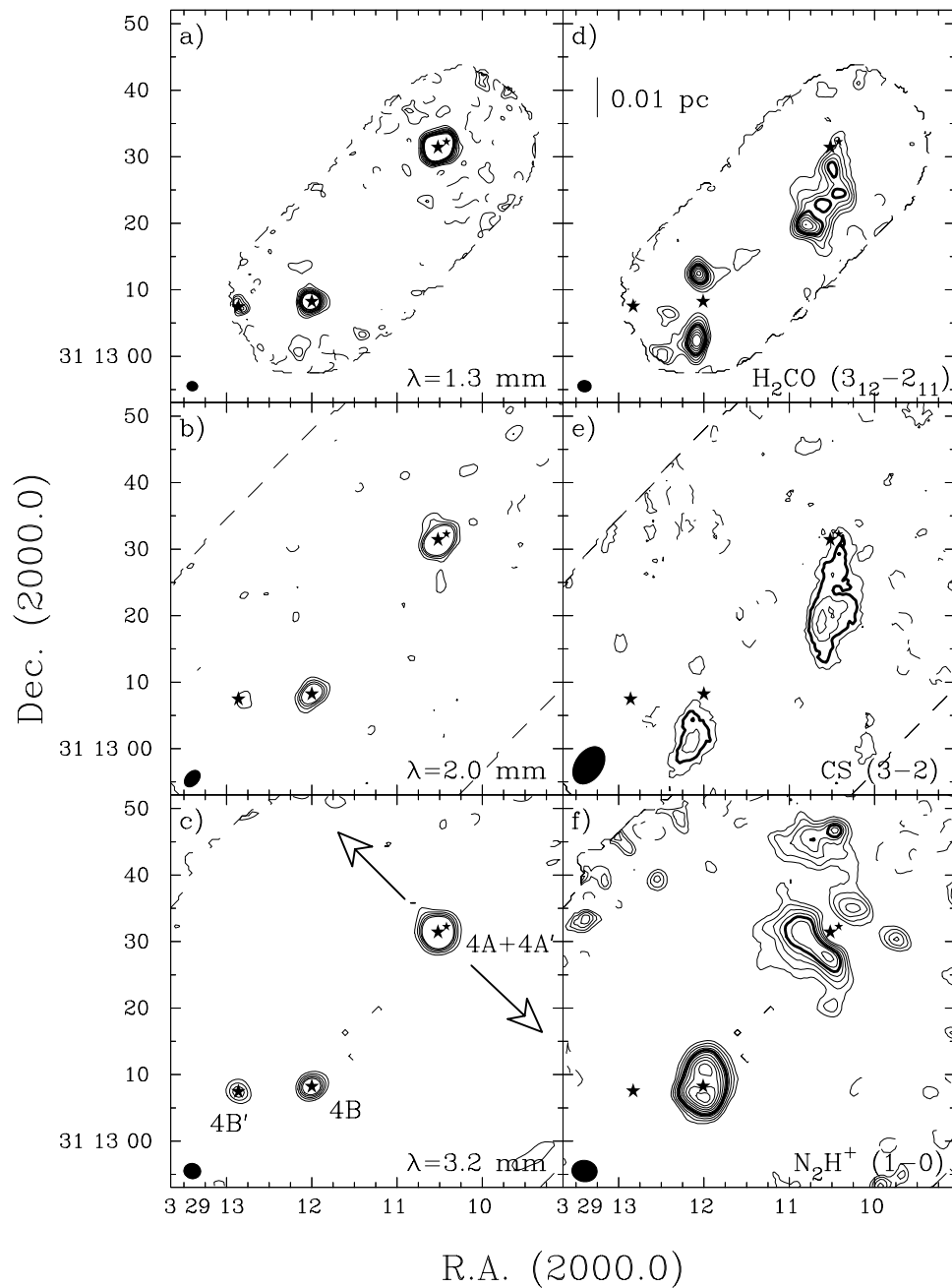
FIG. 1.—Millimeter continuum and line interferometer maps of NGC 1333 IRAS 4. Positions of continuum sources 4A, 4B, and 4B′ at $\lambda = 1.3$ mm are denoted by large black stars, while the position of continuum source 4A′ from Looney et al. (2000) is denoted by a smaller black star. The black ellipses placed in the bottom left of each panel represent the FWHM of the respective synthesized beams. Outer dashed contours represent the masking cutoffs at a specific gain level of the mosaics: 20% for the IRAM PdBI, or 50% for the NRO NMA data. (*a*) $\lambda = 1.3$ mm continuum emission. Plain contours start at 52.5 mJy beam^{-1} (3 σ), increasing in steps of 2 σ to 297.5 mJy beam^{-1}; the dashed contour denotes -52.5 mJy beam^{-1}. (*b*) $\lambda = 2.0$ mm continuum emission. Plain contours start at 42.0 mJy beam^{-1} (3 σ), increasing in steps of 2 σ to 126.0 mJy beam^{-1}; the dashed contour denotes -42.0 mJy beam^{-1}. (*c*) $\lambda = 3.2$ mm continuum emission. Plain contours start at 13.5 mJy beam^{-1} (3 σ), increasing in steps of 2 σ to 49.5 mJy beam^{-1}; the dashed contour denotes -13.5 mJy beam^{-1}. The arrows to the northeast and southwest of 4A + 4A′ denote the directions of the large-scale CO outflow detected by B95. (*d*) Integrated intensity of H$_2$CO 3_{12}–2_{11} emission ("zeroth moment"; see text). The bold contour shows the half-maximum isophote (57 K km s^{-1}), while plain contours step up and down in increments of 1.5 σ (10.5 K km s^{-1}) from this level. (*e*) Integrated intensity of CS 3–2 emission. The bold contour shows the half-maximum isophote (11.1 K km s^{-1}), while plain contours step up and down in increments of 1.5 σ (4.5 K km s^{-1}) from this level. (*f*) Integrated intensity of N$_2$H$^+$ 1–0 emission (over all seven hyperfine components). The bold contour shows the half-maximum isophote (7.6 K km s^{-1}), while plain contours step up and down in increments of 1.5 σ (1.2 K km s^{-1}) from this level.

namely, 4A, 4B, and 4B′ at three different wavelengths. These objects were also detected at greater than 4 σ at $\lambda = 2.2$ and 6.9 mm, but only 4A and 4B were detected at $\lambda = 1.3$ cm. Table 2 lists flux densities measured from our data (see also the Appendix).

Separated from 4A by only $\sim 1''$, 4A′ is not detected distinctly from 4A in our $\sim 2''$–$4''$ resolution maps, but the continuum emission around 4A is extended toward its position. For this paper, we limit discussion of 4A and 4A′ as an unresolved pair rather than consider them individually, i.e.,

TABLE 2
Integrated Flux Densities, Peak Intensities, and Deconvolved Sizes

				DECONVOLVED SIZE	
OBJECT	λ (mm)	S_ν^{total} (mJy)	I_ν^{peak} (mJy beam^{-1})	Major $\times$ Minor Axis (AU $\times$ AU)	P.A. (deg)
4A	1.3	3100 ± 470	$1200 \pm 16.$	920×720	132
	2.0	690 ± 110	$450 \pm 14.$	770×590	129
	2.2	$580 \pm 90.$	$420 \pm 10.$	740×570	119
	3.2	$320 \pm 49.$	200 ± 4.4	790×650	177
	6.9	$26. \pm 4.0$	$16. \pm 0.29$	580×490	138
	13.3	4.7 ± 0.95	3.1 ± 0.27	1100×630	125
4B	1.3	1100 ± 170	$590 \pm 17.$	600×560	151
	2.0	$320 \pm 56.$	$250 \pm 14.$	630×390	119
	2.2	$240 \pm 41.$	$210 \pm 11.$	440×300	151
	3.2	$93. \pm 16.$	$90. \pm 4.5$	$<570 \times <570$	...
	6.9	7.8 ± 1.3	5.8 ± 0.29	630×110	128
	13.3	1.2 ± 0.56	1.0 ± 0.28	$<1400 \times <1400$	...
4B'	1.3	$230 \pm 47.$	$200 \pm 18.$	$<640 \times <640$	...
	2.0	$79. \pm 29.$	$70. \pm 14.$	$<840 \times <840$	...
	2.2	$82. \pm 21.$	$89. \pm 10.$	$<780 \times <780$	...
	3.2	$45. \pm 11.$	$41. \pm 4.5$	$<690 \times <690$	...
	6.9	2.2 ± 0.65	1.9 ± 0.30	$<840 \times <840$	...
	13.3	<0.84	<0.84	...	...

4A = (4A + 4A'). Similarly, we refer to the 4B object as 4B, though it may also be multiple. Furthermore, the nearby source 4C was not observed as it lay outside the fields of view of our PdBI and NMA mosaics, and our VLA images did not have sufficient sensitivity to detect it (based on its flux densities at $\lambda = 3.6$ and 6.0 cm; see Rodríguez et al. 1999).

3.2. H_2CO 3_{12}–2_{11} and CS 3–2

Figures 1d and 1e show that H_2CO and CS are distributed similarly around 4A, 4B, or 4B', but remarkable differences are found between objects. Near 4A, an extended lobe is located to the south to southeast and one or two compact spots are located to the north in both H_2CO and CS. The southern lobe contains four local maxima in the H_2CO data but only two to three maxima in the lower resolution CS data. Near 4B, two single-peaked, compact lobes are seen to the north and south, with similar brightnesses in H_2CO but very different brightnesses in CS. In addition, three less prominent peaks to the east, northwest, and southeast of 4B are detected in H_2CO but not in CS. Finally, no H_2CO or CS emission is detected near 4B'. In our H_2CO map, this source is located at the mosaic edge, making it unclear if the lack of detected H_2CO near 4B' is real or due to reduced sensitivity. In our CS map, however, 4B' is positioned well within the field of view, but no CS is detected near the object.

Figure 2 shows grids of H_2CO 3_{12}–2_{11} spectra from positions centered on 4A and 4B, spaced regularly in 2" increments of R.A. or decl., i.e., ~ 1 FWHM of the synthesized beam. The velocity range of each panel is centered at 6.96 km s^{-1}, the average central velocity determined from N_2H^+ 1–0 data of 4A and 4B (see § 4.3.2), which we consider here to be the systemic velocity of the IRAS 4 group.

Figure 2a reveals that at the 4A position (i.e., the central grid panel), an "inverse P Cygni" line profile of blueshifted emission and redshifted absorption is clearly detected. The absorption feature has a central velocity of 7.6 km s^{-1} and a width of ~ 0.9 km s^{-1} and is not prominent at any other

grid location. The maximum depth of the absorption toward 4A is ~ 9 K, or 1.3 Jy beam^{-1}, approximately equal to the peak intensity of $\lambda = 1.3$ mm continuum emission detected at the same position (see Table 2). With single-dish data, M98 detected asymmetrically blue, single-peaked H_2CO emission with no absorption at the 4A position. North of 4A, the H_2CO spectra are double peaked, with a dip at ~ 7.7 km s^{-1}, and a weak red wing is seen. South of 4A, the H_2CO spectra are single peaked, but a strong blue wing is seen. The emission spot due north of 4A in Figure 1d almost entirely consists of this redshifted wing emission. (The apparent H_2CO emission spot northwest of 4A is incidental map-edge noise.) The extended lobe seen south to southeast of 4A in Figure 1d almost entirely consists of blueshifted wing emission.

Figure 2b reveals an inverse P Cygni line profile at the 4B position (at the center of this grid, defined similarly to Fig. 2a). Here the absorption has a central velocity of 7.9 km s^{-1} and a width of ~ 1.0 km s^{-1}. The maximum depth of the absorption feature toward 4B is ~ 4 K, or 0.57 Jy beam^{-1}, again approximately equal to the peak intensity of continuum emission at $\lambda = 1.3$ mm. In addition, absorption is not prominent at positions offset from the continuum object. M98 also only detected asymmetrically blue, single-peaked H_2CO emission with no absorption below the continuum at the 4B position. Furthermore, spectra to the north of 4B are double peaked and a red wing is seen, like that seen north of 4A and also with a self-absorption at ~ 7.7 km s^{-1}. South of 4B, the line is single peaked and a blue wing is found, similar to the line south of 4A. The bright peaks north or south of 4B seen in Figure 1d predominantly consist of either redshifted or blueshifted wing emission, respectively, and the secondary features seen northwest and southeast of 4B consist of blueshifted and redshifted emission, respectively. (The third emission feature seen in Fig. 1d near 4B is off the eastern edge of the grid in Fig. 2b and has both blueshifted and redshifted emission.)

Line profiles similar to those found for H_2CO 3_{12}–2_{11} in Figure 2 are also seen for the CS 3–2 line at similar posi-

a) 4A: H_2CO $3_{12}-2_{11}$

a) 4A: N_2H^+ $101-012$

b) 4B: H_2CO $3_{12}-2_{11}$

b) 4B: N_2H^+ $101-012$
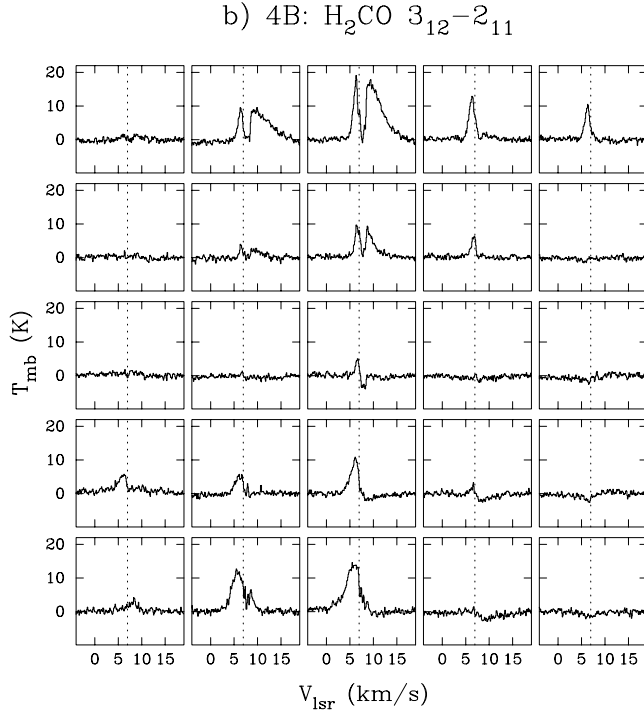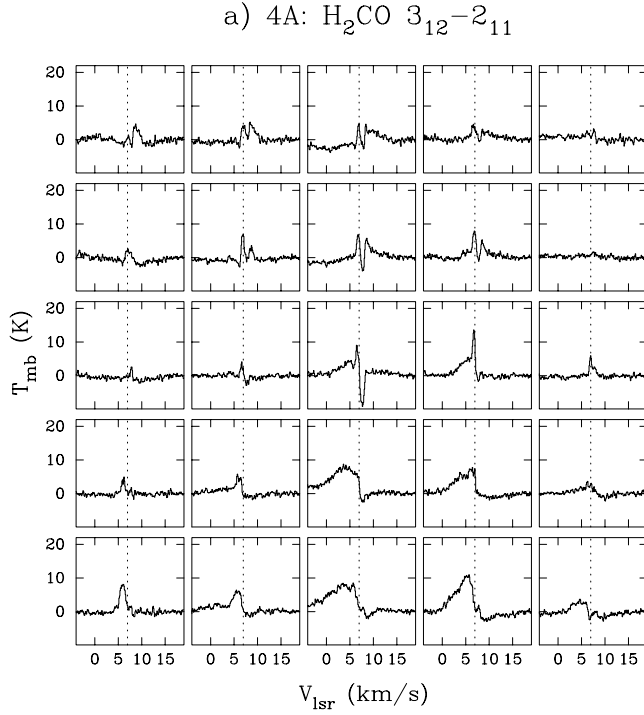

FIG. 2.—Grids of H_2CO $3_{12}-2_{11}$ spectra at selected positions at and around 4A and 4B. In both grids, panels are spaced by 2″ in R.A. or decl., ~1 FWHM of the beam at 225.7 GHz, the H_2CO $3_{12}-2_{11}$ rest frequency, so adjacent panels in the H_2CO grid are independent. The dashed line represents the determined V_{LSR} of the IRAS 4 system of 6.96 km s^{-1}. (a) Panels centered at the 4A position at $\lambda = 1.3$ mm [R.A.(2000) = 03^{h}29^{m}10^{s}5, decl.(2000) = 31°13′31″4]. (b) Panels centered at the 4B position of 4B at $\lambda = 1.3$ mm [R.A.(2000) = 03^{h}29^{m}12^{s}0, decl.(2000) = 31°13′08″2].
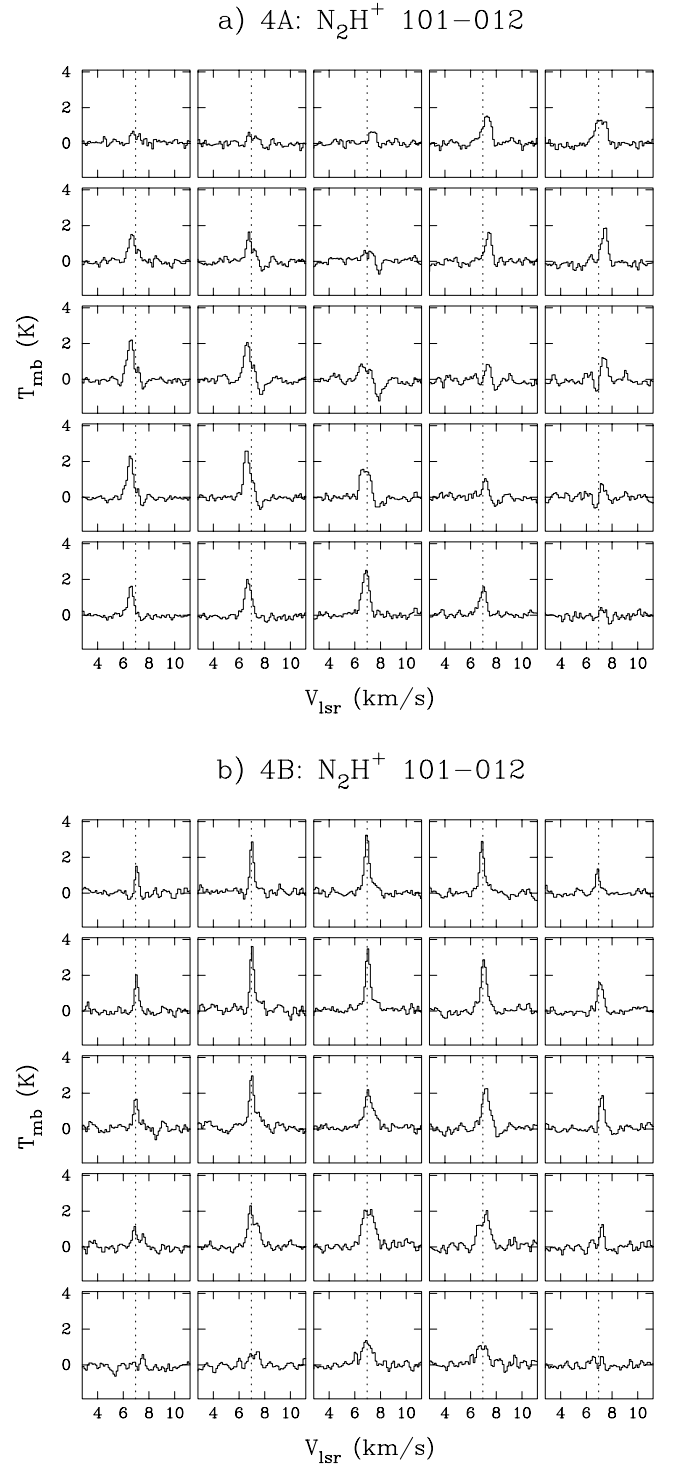
FIG. 3.—Grids of N_2H^+ 1–0 spectra at the same positions at and around 4A and 4B defined for Fig. 2. As a result of the larger beam at 93.17 GHz, the N_2H^+ 1–0 rest frequency, the adjacent panels are not independent, as in Fig. 2. In addition, the velocity range in each panel here is wider relative to that of Fig. 2, although panels in both figures are centered at the same velocity.

tions, including an absorption feature at 7.8–8.0 km s^{-1} in the CS spectrum at 4A and a possible analog at 4B. These data are not shown since they corroborate the H$_2$CO data but are noisier and have lower spatial resolution.

3.3. N$_2$H$^+$ 1–0

Figure 1f shows the integrated intensity (zeroth moment) of N$_2$H$^+$ 1–0 emission around the IRAS 4 objects. These distributions differ significantly from those of H$_2$CO and CS (Figs. 1d and 1e) around each object. However, the spatial distribution of the integrated intensity also differs from object to object. Near 4A, the N$_2$H$^+$ emission is elongated northeast-southwest, extending somewhat symmetrically 10″–15″ around a bisecting channel at position angle (P.A.) $\approx 45°$ containing 4A and 4A′. Near 4B, the N$_2$H$^+$ emission is more compact than that near 4A, although it is slightly elongated north-south. In addition, N$_2$H$^+$ emission is coincident with the 4B object, unlike at 4A (i.e., no bisecting channel is seen in the zeroth-moment map). Near 4B′, N$_2$H$^+$ is not detected, although its position here is well within the field of view, unlike in the H$_2$CO mosaic.

Figure 3 shows grids of spectra of N$_2$H$^+$ 101–012, at the same positions at and around 4A and 4B shown in Figure 2. (For clarity, only the "isolated" hyperfine component of N$_2$H$^+$ 1–0 is shown.) Since the 2″ spacing of panels in Figure 3 corresponds approximately to half-beam spacing at the FWHM of the synthesized beam at 93.2 GHz, neighboring panels are not independent, as in Figure 2. (In addition, the velocity range of these grid panels differs from that of Figure 2 but remains centered at the same systemic velocity.)

Figure 3a reveals (in the central panel) another inverse P Cygni line profile at the 4A position, with absorption of central velocity and width similar to those of H$_2$CO at the same position, i.e., 7.9 and ~ 1 km s^{-1}, respectively. (Absorption seen here in adjacent panels is still coincident with the continuum object as a result of the half-beam, nonindependent grid spacing.) Unlike the H$_2$CO absorption, the peak depth is only ~ 1.2 K, or $\sim 50\%$ the peak continuum intensity of 4A at $\lambda = 3.2$ mm. M98 did not detect absorption of N$_2$H$^+$ 1–0 in their single-dish data at the 4A position. At positions northwest and southeast of 4A, the line is single peaked in emission only with small shifts in central velocity to the red and blue, respectively. No systematic line width variation or wing emission is seen. The bisecting channel at P.A. $\approx 45°$ seen in Figure 1f is noticeable here from the relatively dim emission found in panels on the northeast-southwest diagonal.

Figure 3b shows that an inverse P Cygni line profile is not seen at the position of the 4B object; rather, a fairly symmetric line is found peaking at 7.1 km s^{-1}, near the systemic velocity. (Absorption may be present at ~ 8 km s^{-1} in the grid panel 2″ west of the central position, but this is not suggested in any other adjacent, nonindependent grid panel.) Unlike near 4A, there does not appear to be substantial variations in central velocity over the grid, but the line is dimmer and broader south of 4B and brighter and narrower north of 4B. Like near 4A, there is no evidence for wing emission. M98 detected a similarly shaped single-peaked line profile at the 4B position.

4. DISCUSSION

4.1. Distinct Tracers of Specific Motions

The spectral and spatial distributions of the lines described in § 3 trace quite distinctly specific types of motion within IRAS 4. Infall is traced from the inverse P Cygni profiles detected in H$_2$CO toward both 4A and 4B (and also in CS and N$_2$H$^+$ toward 4A alone). Outflows from 4A and 4B are traced distinctly from infall, at positions offset from the protostellar objects, from H$_2$CO and CS lines with profiles of only bright line wings and no line cores. Rotation of nonoutflowing dense gas around 4A or 4B is traced distinctly from outflow from spatial variations of the central velocity of N$_2$H$^+$, with profiles of only line cores and no line wings. Furthermore, variations of turbulent motions within the nonoutflowing dense gas about 4A and 4B are traced by spatial variations of the line width of N$_2$H$^+$ in the same profiles.

The observed lines distinctly trace specific motions partly because of the differing gas-grain chemistry of the molecular species. B95 suggested that H$_2$CO and CS were depleted in the nonoutflowing gas associated with 4A and 4B, as a result of significant amounts of these molecules adsorbing onto dust grains. Detailed models by Bergin & Langer (1997) of relative abundances in centrally condensed cores of increasing density support this scenario, showing that H$_2$CO or CS may deplete by ≥ 2 orders of magnitude at densities of $n \approx 10^5$ cm^{-3} onto grains with H$_2$O or CO mantles. These models, in turn, also suggest that N$_2$H$^+$ remains at a constant abundance to densities of $\sim 10^6$ cm^{-3}, as a result of the low binding energy of N$_2$, its precursor molecule, to grain mantles. Therefore, we expect that N$_2$H$^+$ traces nonoutflowing dense gas better than H$_2$CO or CS in a suitably dense protostellar core. In contrast, B95 suggested that the enhanced abundances of H$_2$CO and CS found in the line wings were due to significant amounts of these molecules returning to the gas phase from the disruption of grain mantles in the outflows. Moreover, the single-dish data of M97 show that the N$_2$H$^+$ 1–0 components at 4A and 4B have Gaussian profiles, with no emission at the wing velocities of H$_2$CO or CS. Models of molecular abundance variations from postshock chemistry by Bergin et al. (1998) support this contrast, since the increased abundance in outflows of H$_2$O, returned to the gas phase from grain mantles, appears to rapidly deplete N$_2$H$^+$. Therefore, we expect that H$_2$CO or CS traces better outflowing gas than N$_2$H$^+$. Such molecular abundance contrasts are not unique to IRAS 4 and have been observed similarly elsewhere, e.g., the single-dish observations of the L1157 core and outflow by Bachiller & Pérez-Gutiérrez (1997).

Another important reason our data distinctly trace specific motions is their high spatial resolution. For example, interferometers allow detection of the inverse P Cygni profiles because the brightnesses of the continuum objects in the relatively small beams can exceed the brightnesses of line emission from intervening, infalling gas along the line of sight, leading to redshifted absorption. (Blueshifted emission in the inverse P Cygni profiles arises from concentrated gas on the far sides of the protostellar objects.) In addition, the spatial filtering properties of the interferometer can further distinguish specific motions better than single-dish observations, especially at low relative velocities, by selectively sampling the kinematics of compact structures and resolving out confusing, extended emission. For example, outflowing gas is detected more distinctly in interferometer observations of H$_2$CO or CS, beyond abundance differences, because zones of outflowing dense gas are expected to

be more compact, and hence are more easily seen by an interferometer, than the outer, less dense layers of a circumstellar envelope that may still contain abundant H_2CO or CS. On the other hand, interferometers can still detect non-outflowing gas in such an envelope using N_2H^+ because, unlike H_2CO or CS, it remains relatively abundant in the denser and more compact inner regions that are less resolved out than outer regions. (As described below, N_2H^+ may be somewhat depleted relative to "canonical" values in IRAS 4.)

4.2. H_2CO Observations

4.2.1. Infall

Detections of redshifted absorption indicative of infall motions have been made primarily toward high-mass young stellar objects, where the absorption profiles were seen against the continuum emission of bright H II regions in interferometer beams. For example, redshifted absorption was seen toward G10.6−0.4 in NH_3 (1, 1) and (3, 3) by Keto, Ho, & Haschick (1987, 1988; with VLA beams of 3″0 and 0″3 FWHM, respectively). Similar profiles were also detected toward W51:e2 in NH_3 (1, 1) and (2, 2) by Ho & Young (1996; with VLA beams of 2″6–3″8 FWHM), in these transitions plus NH_3 (3, 3) by Zhang & Ho (1997; with VLA beams of 0″2–1″0 FWHM), and in CS 3–2 by Zhang, Ho, & Ohashi (1998; with an NMA 1″1 FWHM beam). Furthermore, an inverse P Cygni profile was noted toward W49A North:G in HCO^+ 1–0 by Welch et al. (1987; with a BIMA ∼7″ FWHM beam).

Toward low-mass young stellar objects, detections of redshifted absorption against continuum emission have been very rare, the only case being the weak inverse P Cygni profile detected in the HCN 1–0 line toward NGC 1333 IRAS 4A by Choi et al. (1999) with a BIMA ∼8″–12″ FWHM beam. (Redshifted absorption is also suggested in their Fig. 1f in the HCN line toward IRAS 4B, and in the HCO^+ 1–0 line toward both objects, but they describe only the HCN line toward 4A as an inverse P Cygni profile.[8])

Figure 4 shows the H_2CO $3_{12}–2_{11}$ line at positions of maximum continuum intensity from 4A and 4B (enlarged from the central panels of Figs. 2a and 3a). These data provide the least ambiguous evidence for infall motions toward low-mass young stellar objects. First, the detection of the absorption here is very strong, given the low channel-to-channel noise of these data. Second, the excitation requirements of the lower energy level of the H_2CO $3_{12}–2_{11}$ transition (i.e., $E_{2_{11}}/k = 7.5$ K) are higher than those of HCN 1–0, suggesting that the absorptions are more likely occurring in warmer gas associated with the young objects rather than in a layer of cooler gas at slightly higher velocity situated along the line of sight (and possibly not associated with the young objects). In addition, the scales probed by these data are smaller than other investigations. At a distance of 350 pc, the linear beam size (FWHM) of the H_2CO data at IRAS 4 is ∼0.003 pc, a factor of ∼4–6 less than the scales probed by Choi et al. (1999) and a factor of ∼2 less than those probed with inverse P Cygni profiles at the more distant, higher mass objects noted above.

To probe conditions in the absorbing gas, the inverse P Cygni profiles toward 4A and 4B were modeled with an
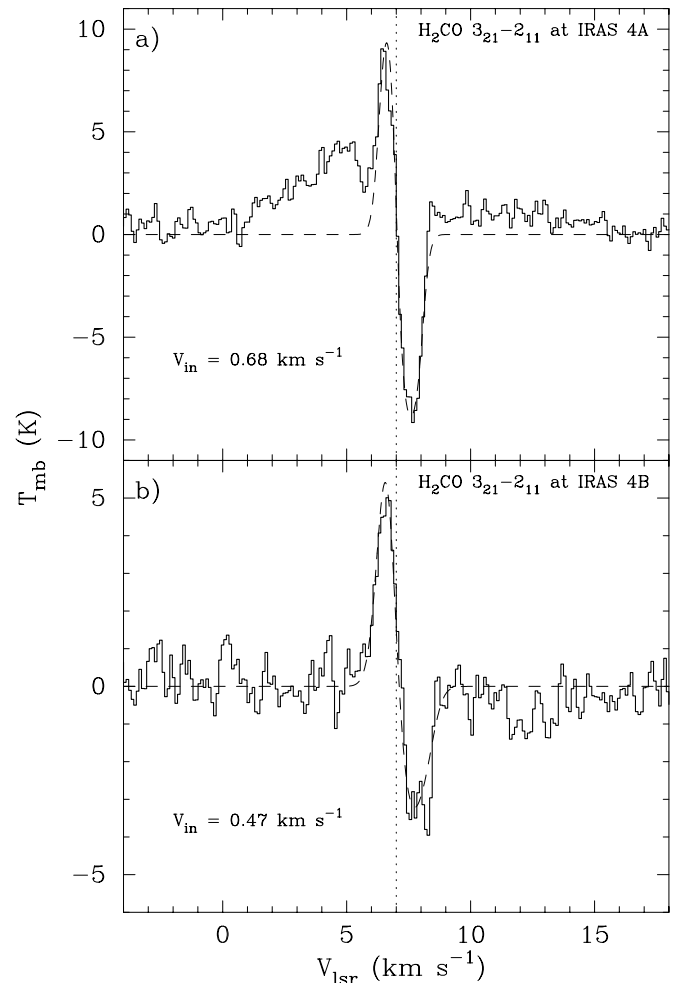

FIG. 4.—H_2CO $3_{12}–2_{11}$ spectra from the IRAM PdBI toward the positions of peak continuum intensity near (a) 4A and (b) 4B. The dotted line denotes the average systemic V_{LSR} of 6.96 km s^{-1}. In each panel, a dashed line shows a spectrum resulting from a simple two-layer model of infall toward each object. Respective model parameters are listed in Table 3.

---

enhanced version of the "two-layer" code used by Myers et al. (1996) to reproduce successfully the appearance of spectral lines from infalling gas toward several protostellar cores (see also Williams & Myers 2000; Lee, Myers, & Tafalla 2001). In this version, two layers, located along the line of sight, each have peak optical depth τ_o, velocity dispersion σ, and approach speed V_{in} toward a continuum source located in between. The continuum source is assumed to be optically thick with a Planck temperature J_c, where J_c is related to the blackbody temperature T_c at frequency v by $J_c = T_o/[\exp(T_o/T_c) − 1]$, where $T_o = hv/k$, h is Planck's constant, and k is Boltzmann's constant. The continuum source also fills a fraction Φ of the telescope beam area. The "front" layer between source and observer has a Planck excitation temperature J_f, while the "rear" layer behind the source has a Planck excitation temperature J_r. The rear layer is illuminated by the cosmic background radiation of Planck temperature J_b.

For this system, the observed line brightness temperature at velocity V can be written as

$$\Delta T_B = (J_f − J_{cr})[1 − \exp(−\tau_f)] + (1 − \Phi)(J_r − J_b)$$
$$\times [1 − \exp(−\tau_r − \tau_f)], \qquad (1)$$

---

[8] An inverse P Cygni profile of the ^{13}CO (2–1) line toward 4A has been also recently detected by Z. T. Webster & W. J. Welch (2000, private communication) with a BIMA 6″7 FWHM beam.

where

$$J_{\rm cr} = \Phi J_c + (1 - \Phi) J_r \, , \qquad (2)$$

and

$$\tau_f = \tau_o \exp\left[\frac{-(V - V_{\rm in} - V_{\rm LSR})^2}{2\sigma^2}\right] , \qquad (3a)$$

$$\tau_r = \tau_o \exp\left[\frac{-(V + V_{\rm in} - V_{\rm LSR})^2}{2\sigma^2}\right] . \qquad (3b)$$

In this model, the line profile can be understood very simply from equation (1) as the linear sum of a broad positive profile centered on $V_{\rm LSR}$ (i.e., the second term on the right-hand side) and a narrow negative profile centered on $V_{\rm LSR} + V_{\rm in}$ (i.e., the first term on the right-hand side). If the systematic motion of the layers is inward (i.e., $V_{\rm in} > 0$), equation (1) implies that the resulting profile shows red absorption or "infall asymmetry." If the front layer is cooler than the continuum source and rear layer by a relatively small temperature difference $J_f - J_{\rm cr}$, the asymmetric profile shows "self-absorption" but remains positive at all velocities. As this temperature difference increases, the profile becomes more asymmetric and its "dip" goes below the spectral baseline.

Equations (1)–(3) are essentially the same as equations (1) and (2) of Myers et al. (1996), except that the emission from an optically thick central source is now included. This model is intended to give the simplest possible description of a contracting or expanding system that can reproduce the observed line profiles. Therefore, it gives only the crudest picture of the optical depth and excitation temperature of the absorbing and emitting gas. However, the model is still useful for comparing the characteristic velocity $V_{\rm in}$ from one line profile to the next, since the ratio $V_{\rm in}/\sigma$ is most important to setting the line profile for any model of a contracting system (Leung & Brown 1977).

In addition to the observed spectra, Figure 4 shows model inverse P Cygni profiles that successfully reproduce those observed. The respective model parameters are listed in Table 3. Infall speeds of $V_{\rm in} = 0.68$ and 0.47 km s^{-1} are obtained toward 4A and 4B, respectively. (The blue wing in the 4A spectrum is likely from outflow and so is not fitted by the model.) Using essentially the same two-layer model (but without a continuum object), M98 found a $V_{\rm in}$ of only 0.11 km s^{-1} for the IRAS 4 region from the same H_2CO line. The difference between these results is likely because the spectrum modeled by M98 was obtained with a resolution coarser by a factor of ~ 6 than those shown here and consisted of data averaged over the FHWM of their single-dish integrated intensity map, i.e., over a projected distance from the source of ~ 0.04 pc. The resulting emission spectrum included data from positions offset from 4A and 4B with gas having possibly lower apparent infall velocities due to projection, whereas the inverse P Cygni profile traces material along the line of sight to 4A or 4B with minimal projection effects.

The inverse P Cygni profiles alone cannot demonstrate whether the infalling material consists of dense gas individually surrounding 4A or 4B, or from a common layer surrounding both objects, since infalling material at projected locations between 4A and 4B is not traced. However, the difference between $V_{\rm in}$ toward 4A and 4B is significant in that the range of $V_{\rm in}$ able to reproduce well each spectrum is only a few hundredths of kilometers per second, if all other

parameters are kept fixed. Different values of $V_{\rm in}$ toward 4A and 4B suggest that the absorptions arise in dense gas residing around each source rather than in a layer common to both objects, where presumably more similar velocities toward 4A and 4B would be found.

From simple gravitational arguments, the line-of-sight speeds implied by the absorptions allow crude estimates of the masses of the 4A and 4B objects, assuming that the infall speeds $V_{\rm in}$ arise from the velocity gain of gas free-falling from rest at $r = \infty$ to $r_{\rm in}$, or

$$M = \frac{V_{\rm in}^2 r_{\rm in}}{2G} = 1.2\left(\frac{V_{\rm in}}{1.0 \text{ km s}^{-1}}\right)^2 \left(\frac{r_{\rm in}}{0.01 \text{ pc}}\right) M_\odot . \qquad (4)$$

To obtain (an upper limit of) $r_{\rm in}$, the mass obtained from equation (4) can be equated with that within a sphere of radius $r_{\rm in}$ and mean density n, i.e., $M = (4/3)\pi r_{\rm in}^3 n\mu m_{\rm H}$, with μ equal to the mean molecular weight (2.32) and $m_{\rm H}$ equal to the mass of hydrogen. We assume $n = 1.3 \times 10^6$ cm^{-3}, the critical density of the H_2CO 2_{11}–1_{10} line, a sufficient density for substantial population of the 2_{11} energy level of H_2CO, determined at $T_k = 30$ K (Green 1991) since B95 estimated a kinetic temperature of nonoutflowing gas around 4A of 20–40 K. Accordingly, the values of $V_{\rm in}$ obtained for 4A and 4B yield values for $r_{\rm in}$ of 0.013 and 0.0091 pc, respectively, or $7\rlap{.}''7$ and $5\rlap{.}''4$, respectively, at the assumed distance of IRAS 4. These radii are smaller by factors of 1.0–1.7 than those obtained using integrated N_2H^+ 1–0 emission (see Fig. 1f) to trace the projected extents of dense gas around 4A and 4B, which is consistent given the lower critical density of that transition.[9] Using equation (4), the masses interior to the respective values of $r_{\rm in}$ are 0.71 and 0.23 $M_\odot$ for 4A and 4B, reasonable values given the moderate luminosities of these objects and their location within a region of low-mass star formation.

Mass accretion rates, $\dot{M}_{\rm in}$, can be estimated toward 4A and 4B using the simple expression $\dot{M}_{\rm in} = 4\pi r_{\rm in}^2 \mu m_{\rm H} n V_{\rm in}$, or

$$\dot{M}_{\rm in} = 9.6 \times 10^{-5}\left(\frac{r_{\rm in}}{0.01 \text{ pc}}\right)^2 \left(\frac{n}{1.3 \times 10^6 \text{ cm}^{-3}}\right)$$
$$\times \left(\frac{V_{\rm in}}{1.0 \text{ km s}^{-1}}\right) M_\odot \text{ yr}^{-1} , \qquad (5)$$

assuming spherical symmetry of the infall. With the values of $V_{\rm in}$, n, and $r_{\rm in}$ described above, we estimate $\dot{M}_{\rm in} = 1.1 \times 10^{-4}$ $M_\odot$ yr^{-1} for 4A and 3.7×10^{-5} $M_\odot$ yr^{-1} for 4B, using equation (5). Assuming that these rates are constant, accretion timescales $t_{\rm acc}$ can be then estimated by dividing the masses found above with the accretion rates. Such a calculation yields $t_{\rm acc} = 6.5 \times 10^3$ and 6.2×10^3 yr for 4A and 4B, respectively, remarkably similar and well within the $t_{\rm acc} < 10^4$ yr surmised for Class 0 objects.

If the isothermal sound speed of this gas can be approximated as $V_{\rm rms} = (kT_k/\mu m_{\rm H})^{1/2}$ and $T_k \approx 30$ K, the values obtained here for $V_{\rm in}$ suggest that the infall motions toward 4A or 4B are supersonic, by factors of 2.1 and 1.4, respectively. Given that the magnetic field strength is poorly known in IRAS 4, however, it is not clear if the infall motions are also sub- or super-Alfvénic. From a virial

---

[9] Nonoutflowing H_2CO in emission, i.e., over the velocities traced by N_2H^+, is difficult to see around 4A and 4B, possibly as a result of low abundances or the relative brightness of the outflows.

TABLE 3

"Two-Layer" Model Parameters for Inverse P Cygni Profiles[a]

Object	τ_o	Φ	J_c (K)	J_f (K)	J_r (K)	V_{LSR} (km s^{-1})	σ (km s^{-1})	V_{in} (km s^{-1})
4A......	2.0	0.3	45	3	19	6.85	0.34	0.68
4B......	1.6	0.3	30	3	20	7.13	0.51	0.47

[a] See Fig. 4 for model profiles.

theorem argument, Akeson et al. (1996) estimated large magnetic field strengths associated with 4A of 5–8 mG, suggesting that the infall flows are very sub-Alfvénic. However, the summary of actual magnetic field measurements (of other various molecular clouds) by Crutcher (1999) suggests that these values may be too large by factors of ~ 10–100. If the infall motions are occurring exactly at the Alfvén speed [i.e., $V_A = B/(4\pi\mu n m_H)^{1/2}$ with $n = 1.3 \times 10^6$ cm^{-3}], the required magnetic field strengths near 4A and 4B would be 540 and 370 μG, respectively.

The two-layer models used to compute the line profiles seen in Figure 4 neglect the radial variations in density, temperature, and velocity expected within protostellar envelopes. Therefore, these results are too simple to be definitive but provide motivation for more observations and models of inward motions. It will be useful to make more detailed, Monte Carlo models of radiative transfer through envelopes, of the H_2CO line from these and other Class 0 objects.

4.2.2. Outflow
4.2.2.1. Outflow Morphologies and Origins

Figure 5 shows channel maps of H_2CO 3_{12}–2_{11} emission near 4A, revealing the underlying structure of the blue 4A outflow lobe better than the integrated intensity map (Fig. 1d). In channel maps, the blue lobe consists of two prominent features south by southwest and southeast of 4A. Increasing in relative velocity, emission from the first feature is first seen at 6.5 km s^{-1}, and it peaks at increasing angular separations from 4A in a Hubble law manner reminiscent of other protostellar outflows (see Bachiller 1996). At 2.0 km s^{-1}, however, the angular separations of the peaks of this feature shift to the southeast with increasing velocity out to the band edge, -10 km s^{-1}. The second feature is first seen at 6.8 km s^{-1} and moves south and west with increasing relative velocity in a manner less consistent with a Hubble law. Together, these features resemble cavity walls of an outflow seen at increasing relative velocities. In contrast to Figure 1d, the channel maps suggest that the 4A blue lobe has an overall P.A. of $\sim 160°$, and its north-south appearance in Figure 1d is due to the relative brightness of the western cavity wall. Figure 5 also shows dense gas outflowing from 4A', the binary companion to 4A, at low relative velocities along the south by southwest feature, but dense gas appears to be outflowing instead from 4A at higher relative velocities.

Our H_2CO data reveal a systematic decrease in the P.A. of the 4A outflow axis with scale that could be due to precession of the 4A outflow axis (i.e., a systematic change in its P.A. with time). Single-dish CS data from B95 and Lefloch et al. (1998) show the blue lobe oriented southwest at separations greater than 35″ from 4A but oriented south at separations 15″–35″ from 4A. Our data show that this trend

continues to smaller separations, since the blue lobe is oriented to the southeast at less than 15″ offsets from 4A. Such precession may be due to the binarity of 4A, if the gravitational action of 4A' on 4A is strong enough (or vice versa). The inherent periodicity of precession, however, suggests that outflow gas will be distributed periodically in P.A. at even larger scales, and indeed such evidence may exist in recent CO maps of NGC 1333. For example, a CO 3–2 JCMT map of Knee & Sandell (2000) shows what may be the northern red lobe of the 4A outflow curving north of IRAS 4, from a P.A. of 45° to a P.A. of 0° over 3′–4′. In addition, the CO 1–0 BIMA mosaic of NGC 1333 by Plambeck & Engargiola (1999) faintly shows possible emission from the 4A outflow at large scales, curving symmetrically over several arcminutes from 4A in an S shape. However, maps that are more sensitive than these are required to determine conclusively if this distant emission is actually related to the 4A outflow. (As this paper was being revised after submission, a periodicity in the P.A. of the 4A outflow was seen by Choi 2001. However, the amplitude suggested here is larger by a factor of ~ 10.)

The difference in integrated intensity between sides of the 4A blue lobe could be understood if the outflow is precessing, as dense gas surrounding 4A may be cleared out in some directions more than others by a precessing outflow. For example, the emission from the western wall of the outflow cavity shown in Figure 5 may extend to higher relative velocities than the eastern wall if the outflow has encountered less mass to the west, a direction along which gas may have been most recently cleared out by the precessing outflow. This scenario may also explain why the terminus of the outflow cavity appears to shift to the west with increasing relative velocity.

Figure 6 shows channel maps of the dense gas features near 4B, revealing the underlying structure of its outflow. Here all features are found at increasingly large positional offsets from 4B with increasing relative velocity in a Hubble law manner, except the feature east of 4B, which moves in the opposite sense. Correspondingly, the latter feature may be emission from dense gas outflowing from 4B'. (Our mosaic does not cover area east of 4B' where other possible outflow features from 4B' could reside.)

The red features to the north and southeast and the blue features to the south and northwest seen in Figure 6 together suggest an X shape, possibly indicative of outflow cavity walls similar to those surmised for the 4A blue lobe. In this case, the 4B dense gas outflow may consist of two lobes, one situated at a north by northwest P.A. (i.e., $\sim 345°$) with an opening angle of $\sim 45°$, and another at a south by southeast P.A. (i.e., $\sim 160°$) with an opening angle of $\sim 30°$. The peculiar appearance of both red and blue outflow emission on the same sides of 4B then may be due to the 4B outflow being inclined from the plane of sky at an angle less than, e.g., the $\sim 30°$ opening angle of the narrower lobe. An
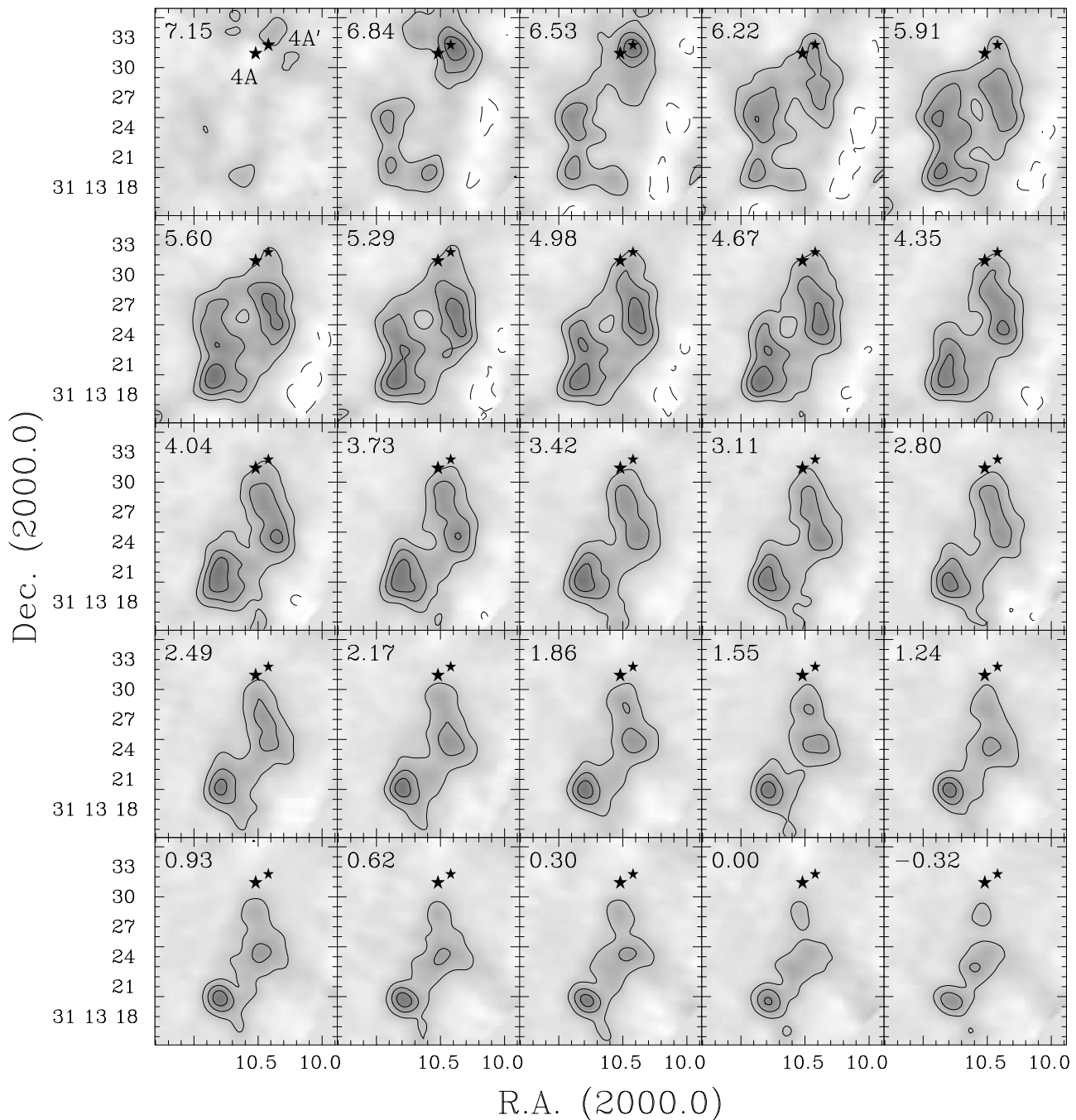
Fig. 5.—Channel maps of H_2CO 3_{12}–2_{11} emission revealing the underlying structure of the southern blue lobe of the 4A dense gas outflow. Each channel is the mean of three channels of the original data cube and has a channel width of 0.3113 km s^{-1}. The velocity of a given panel is shown at the upper left in km s^{-1}; only a fraction of channels blueward of the systemic velocity are shown. Continuum positions of 4A and 4A′ are denoted by large stars and small stars, respectively. Solid contours begin at 3.5 K and increase in steps of 3.5 K, and dashed contours begin at −3.5 K and decrease in steps of −3.5 K. The gray scale ranges from −3.5 to 28.2 K.

alternative is that the brighter and dimmer pairs of symmetric red and blue dense gas outflow features are each independent outflows, with a projected difference in the orientation of their axes of ∼30°–45°, driven by unresolved objects within 4B. As with 4A, the H_2CO emission may still trace cavity walls in this case, but here they may be unresolved. A close companion to 4B is suggested by the subarcsecond resolution continuum data of Lay et al. (1995) and Looney et al. (2000), but this has not yet been confirmed.

4.2.2.2. Physical Properties of Outflows

Physical properties of the outflowing dense gas can be estimated from the H_2CO data, with some assumptions. To estimate the mass of outflowing gas, local thermodynamic equilibrium (LTE) was assumed and line emission was assumed to be optically thin, although these assumptions are likely not valid within dense gas outflows. To obtain deprojected relative gas velocities, both outflows were assumed to originate at the V_{LSR} of 4A or 4B (see § 4.3.2) and are inclined 10° from the plane of sky as a result of the low
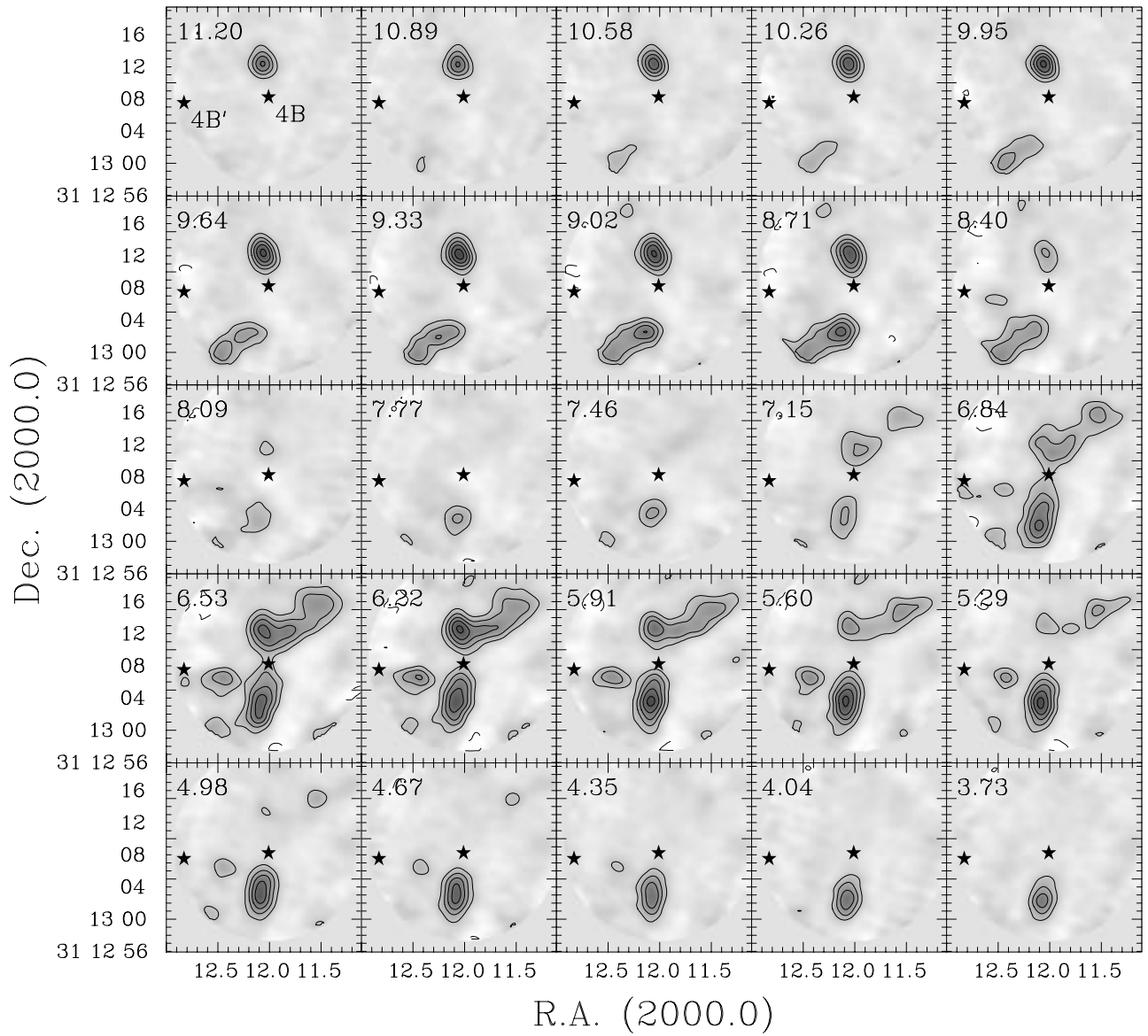
FIG. 6.—Channel maps of H_2CO $3_{12}-2_{11}$ emission depicting the red and blue lobes of the 4B dense gas outflow. Channel width, contours, gray scales, and symbols are the same as described for Fig. 5, except that stars denote the continuum locations of 4B (*near center*) and 4B′ (*to the left*). In addition, an equal number of channels redward and blueward of the systemic velocity of 4B are shown.

spatial coincidence of their red and blue lobes. In addition, excitation temperature and H_2CO abundance values of $T_{ex} = 50$ K and $X(H_2CO) = 1.8 \times 10^{-7}$ or 4.3×10^{-7} were assumed for 4A or 4B, respectively, as derived by B95 from wing emission.

Rebinning the original data cube to channels of width $\Delta V = 0.31$ km s^{-1} (approximately the thermal broadening FWHM of H_2CO at 50 K, to obtain independent velocity channels l), the total gas mass of a given outflow feature k, M_k, can be estimated as

$$M_k = \frac{Z(T_{ex})}{g_j e^{-hv/kT_{ex}}} \frac{\mu m_H}{X(H_2CO)} \sum_l^{\text{channels}} \int_{\Omega_{kl}} \frac{S_v^{kl} \Delta V}{A_{ji} hv} D^2 \, d\Omega , \quad (6)$$

where S_v^{kl} and Ω_{kl} are the average flux density and deconvolved area of feature k in channel l obtained from two-dimensional Gaussian fits. (The projected distance to the nearest continuum object was also obtained from Gaussian fitting.) About six features were identified by eye within each

of the 4A and 4B outflows, based on their $\geq 4 \sigma$ peak intensities and persistence in several adjacent channels. In addition, A_{ji} is the Einstein A-coefficient of the $3_{12}-2_{11}$ line, v is the line frequency, D is the assumed distance to IRAS 4, $Z(T_{ex})$ is the partition function of H_2CO at T_{ex}, and g_j is the degeneracy of the 3_{12} level.

Masses (M_{out}) were obtained by summing equation (6) over all features. Momenta (P_{out}) or kinetic energies (E_{out}) were obtained by summing the products of mass and relative deprojected velocity per channel, or the products of half the mass and the square of the relative deprojected velocity per channel, respectively, over all features. A characteristic timescale t was determined as the time for mass of a given feature at a given deprojected relative velocity to have traveled to a deprojected distance. (Given the extended nature of mass in each channel, t should not be mistaken for the actual time that all mass in the channel took to travel from the continuum source.) Dividing the momenta and kinetic energies per channel by these timescales per channel and summing over channels and features yielded total charac-

teristic momentum fluxes ($F_{\rm H_2CO}$, or forces) and mechanical luminosities ($L_{\rm mech}$, or powers) of the outflows.

The total derived masses for the 4A and 4B dense gas outflows are 6.9×10^{-4} and 1.5×10^{-4} $M_\odot$, respectively. Table 4 lists these and the other physical properties derived for each dense gas outflow. The two brightest features associated with 4A and 4B contribute, respectively, 45% and 43% of $M_{\rm out}$. Note that values for 4A listed in Table 4 include only the blue lobe of the 4A dense gas outflow, so total properties of the entire 4A dense gas outflow may be larger than those listed by a factor of ~ 2, assuming that the flow is symmetric, e.g., for a total $L_{\rm mech}$ of 0.25 $L_\odot$ yr^{-1}.

Quantities in Table 4 for the 4A southern blue lobe alone exceed those of all the lobes of the 4B dense gas outflow by factors of 5–17. These differences may be significant if both outflows have similar low inclination angles, but this is a very uncertain assumption. For example, the mechanical luminosity, $L_{\rm mech}$, of the 4A blue lobe would decrease by a factor of ~ 90 if the inclination of the flow were 45° instead of 10°, as a result of the intrinsically large dependence on tan i. Differences between the 4A and 4B dense gas outflow characteristics could be expected from differences in the photon luminosities of the protostellar sources. Millimeter wavelength luminosities of 4A and 4B, obtained by integrating continuum flux densities in Table 2 and those at $\lambda = 450$ and 850 μm by Sandell & Knee (2001), are 0.24 and 0.12 $L_\odot$, respectively, only a factor of ~ 2 different. Other factors, therefore, may also be relevant.

Our values of $M_{\rm out}$, $P_{\rm out}$, and $E_{\rm out}$ for the 4A blue lobe are factors of ~ 60–80 less than values derived for the same lobe by Knee & Sandell (2000), assuming their inclination angle (45°) and distance (220 pc). These differences are likely because the CO 3–2 data of Knee & Sandell (2000) (from the JCMT with a 14″ FWHM beam) have greater sensitivity to large quantities of lower density gas [i.e., $n_{\rm cr}$(CO 3–2) $\approx 10^4$ cm^{-3}], suggesting that dense gas (as seen by the H$_2$CO line) is relatively insignificant in terms of the total mass, momentum, and energy of the molecular outflow, comprising less than 2% of these quantities. However, the momentum flux and mechanical luminosities we derive are only factors of ~ 10 less than those derived by Knee & Sandell (2000) for the 4A blue lobe, indicating that the dense gas has greater significance in the total force and power of the 4A outflow.

4.3. N$_2$H$^+$ Observations

As discussed above, the N$_2$H$^+$ molecular ion can be relatively abundant in nonoutflowing dense gas around protostellar objects, and the optical depth of its transitions can be low in all but the densest cases (e.g., L1544; see Williams et al. 1999). In addition, the N$_2$H$^+$ 1–0 transition has seven hyperfine components from which the total brightness temperature ($T_b^{\rm tot}$), the central line velocity ($V_{\rm LSR}$), and the line width (ΔV) can be estimated to good accuracy via simultaneous hyperfine structure fitting. These quantities can be used to estimate the mass of nonoutflowing dense gas around 4A and 4B and probe its rotational and incoherent motions.

Figure 7 shows the values of $T_b^{\rm tot}$, $V_{\rm LSR}$, and ΔV obtained from fitting the hyperfine structure of the N$_2$H$^+$ line around 4A and 4B, using the HFS routine of CLASS (see Caselli, Myers, & Thaddeus 1995). Values of ΔV shown were obtained by deconvolving the measured ΔV with the 0.16 km s^{-1} velocity resolution of the PdBI data. Typical errors from HFS fitting per pixel for $T_b^{\rm tot}$, $V_{\rm LSR}$, and ΔV were 0.94

K, 0.015 km s^{-1}, and 0.032 km s^{-1}, respectively. The quantities shown in Figure 7 are restricted to those recovered from pixels containing data where the peak intensity of the brightest hyperfine component (i.e., N$_2$H$^+$ 123–012) was ≥ 5 times the rms of the respective spectral baseline. With this criterion, regions of dense gas surrounding each object are defined, similar in extent to those obtained by the lowest contour of Figure 1f from an integrated intensity criterion.

In Table 5, the mean, rms, minimum, and maximum values of $T_b^{\rm tot}$, $V_{\rm LSR}$, and ΔV in the nonoutflowing dense gas surrounding 4A and 4B are summarized. To obtain these values, the fields shown in Figure 7 were rebinned into images with pixels 4″.0 $\times$ 3″.5 in size, about the area of the beam, so beam-averaged quantities at spatially independent locations could be examined. (Pixels not meeting the criterion for inclusion in Fig. 7 were also not included in the rebinning.) Around 4B, the mean value of $T_b^{\rm tot}$ is $\sim 60\%$ larger than it is around 4A, but the mean values of $V_{\rm LSR}$ and ΔV are similar in both cases. However, the rms of $V_{\rm LSR}$ for the nonoutflowing dense gas around 4A is ~ 4 times larger than that for the same gas around 4B, a point discussed further in § 4.3.2.

4.3.1. Column Densities and Masses

With quantities obtained from hyperfine structure fitting, the column density of N$_2$H$^+$, N(N$_2$H$^+$), in a given pixel around 4A and 4B can be estimated. Without unique estimates of $T_{\rm ex}$ and $\tau_{\rm tot}$, however, we assume $T_{\rm ex} = 10$ K $\gg hB/3k$, $T_{\rm bg} = 2.73$ K.[10] In addition, we assume that the line is optically thin (i.e., $T_b^{\rm tot} \approx T_{\rm ex}\tau_{\rm tot}$), which is supported by the symmetric appearance of the line over the regions shown in Figure 7. Following similar estimates by Womack et al. (1992), but with these assumptions,

$$N({\rm N_2H^+}) \approx \frac{10^5}{1.06(J+1)} \frac{3h}{8\pi^3\mu^2} \frac{k(T_b^{\rm tot})}{hB}$$
$$\times \frac{e^{E_J/kT_{\rm ex}}}{(1 - e^{-h\nu/kT_{\rm ex}})} \Delta V \, , \qquad (7)$$

where J is the upper rotational level (1), μ is the dipole moment of the N$_2$H$^+$ molecular ion (3.40 D; Green, Montgomery, & Thaddeus 1974), B is the rotational constant of N$_2$H$^+$ (46.586702 GHz; Caselli et al. 1995), E_J is the upper level energy ($= h\nu$, where $\nu = 93.1734035$ GHz; Caselli et al. 1995), and $T_b^{\rm tot}$ and ΔV come from HFS fits. (Note that units for ΔV are km s^{-1}.)

From equation (7), mean values of N(N$_2$H$^+$) in the nonoutflowing dense gas around 4A and 4B of 2.4×10^{12} and 3.9×10^{12} cm^{-2} are found, respectively. Table 5 also lists the rms, minimum, and maximum values for N(N$_2$H$^+$) obtained for this gas around each protostellar object. [Decreasing $T_{\rm ex}$ to 5 K reduces the values of N(N$_2$H$^+$) in Table 5 by only factors of $\sim 5\%$, but increasing $T_{\rm ex}$ to 20 K increases them by factors of $\sim 40\%$–50%.] The mean column densities of nonoutflowing dense gas around both objects are similar, although that of the gas around 4B is $\sim 60\%$ larger than that around 4A. These values are 2.5–5 times larger than the N(N$_2$H$^+$) of 0.95×10^{12} cm^{-2} obtained from the mean N$_2$H$^+$ spectrum of IRAS 4 from single-dish data of M98, under the same assumptions. Maximum column densities listed in Table 5 are 5–8 times

---

[10] $T_{\rm bg}$ is much larger at the positions coincident with the peak continuum intensity, but since this is only significant for relatively few pixels, that difference is ignored here.

TABLE 4

PHYSICAL QUANTITIES OF MASS FLOWS IN NGC 1333 IRAS 4

Derived Quantity	Abbreviation	IRAS 4A[a]	IRAS 4B[b]
Infall[c]:			
Mass accretion rate ($M_\odot$ yr^{-1})	$\dot{M}_{in}$	1.1×10^{-4}	3.7×10^{-5}
Outflow[d]:			
Mass ($M_\odot$)	M_{out}	6.9×10^{-4}	1.5×10^{-4}
Momentum ($M_\odot$ km s^{-1})	P_{out}	1.6×10^{-2}	1.6×10^{-3}
Kinetic energy (ergs)	E_{out}	4.9×10^{42}	3.2×10^{41}
Momentum flux ($M_\odot$ km s^{-1} yr^{-1})......	F_{H_2CO}	4.2×10^{-5}	3.2×10^{-6}
Mechanical luminosity ($L_\odot$)	L_{mech}	1.3×10^{-1}	7.4×10^{-3}

[a] Southern blue lobe only.

[b] Includes contribution from eastern blue lobe, some of which may originate from 4A′; see text.

[c] Derived from very uncertain r_{in}; see text.

[d] For dense gas in outflow only; assumes outflow inclination angle of 10° for both 4A and 4B.

larger than the latter value. [The $N(N_2H^+)$ quantities listed in Table 5 are actually lower limits, given the assumption of $\tau_{tot} \to 0$, but the quantities should not vary much from those listed if $\tau_{tot} < 1$ as expected.]

With $N(N_2H^+)$, the masses of nonoutflowing dense gas traced by N_2H^+, M_{gas}, can be estimated by assuming that the emission originates from gas local to 4A or 4B and not from gas distributed along the line of sight. With this
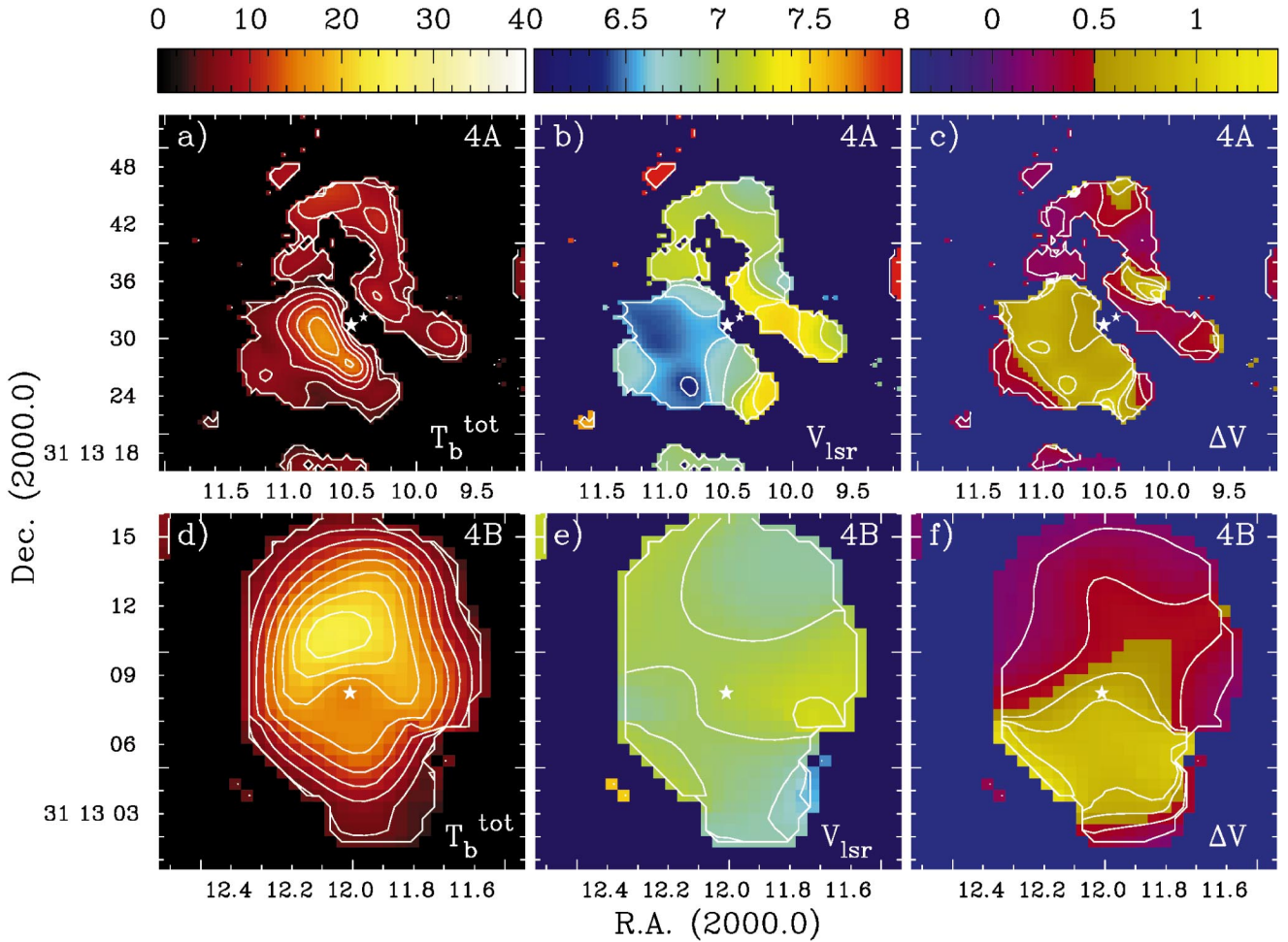

FIG. 7.—Spatial distribution of T_B^{tot}, V_{LSR}, and ΔV of the N_2H^+ 1–0 line around IRAS 4A and 4B, obtained by fitting the seven hyperfine components of the line simultaneously with the HFS fitting routine of CLASS. Only positions where the peak intensity of the brightest hyperfine component was ≥ 5 times the spectral baseline rms are shown, and data at other positions have been blanked. The positions of continuum objects 4A, 4A′, and 4B are represented by stars and are the same positions as denoted in Fig. 1. (a) Distribution of T_B^{tot} around 4A, where the color scale is defined from 0 to 40 K, and contours begin at 2.5 K and continue in increments of 2.5 K to 40.0 K. (b) Distribution of V_{LSR} around 4A, where the color scale is defined from 6.0 to 8.0 km s^{-1}, and contours begin at 6.2 km s^{-1} and increase in increments of 0.2 km s^{-1} to 7.8 km s^{-1}. (c) Distribution of ΔV around 4A, where the color scale is defined from 0.1 to 1.5 km s^{-1}, and contours begin at 0.2 km s^{-1} and increase in increments of 0.2 km s^{-1} to 1.4 km s^{-1}. (d) Distribution of T_B^{tot} around 4B, with the same color scale and contour levels defined for (a). (e) Distribution of V_{LSR} around 4B, with the same color scale and contour levels defined for (b). (f) Distribution of ΔV around 4B, with the same color scale and contour levels defined for (c).

TABLE 5

N$_2$H$^+$ LINE PROPERTIES DERIVED FROM HYPERFINE STRUCTURE FITS

	4A				4B			
VALUE	Mean	rms	Min	Max	Mean	rms	Min	Max
T_B^{tot} (K)	7.8	2.1	3.6	13.	12.	4.4	4.8	21.
V_{LSR} (km s^{-1})................	6.95	0.359	6.48	8.2	6.98	0.0928	6.75	7.38
ΔV(km s^{-1})	0.49	0.17	0.21	0.83	0.50	0.20	0.16	0.81
N(N$_2$H$^+$) (10^{12} cm^{-2})......	2.4	1.2	0.54	5.1	3.9	1.9	0.77	7.7

assumption,

$$M_{gas} = \frac{\mu m_H}{X(N_2H^+)} D^2 \int_{\Omega_s} N(N_2H^+)d\Omega , \qquad (8)$$

where μ, m_H, and D are the same as for equation (6), but Ω_s is the solid angle subtended by the dense gas traced by N$_2$H$^+$ around each object, and $X(N_2H^+)$ is the fractional abundance of N$_2$H$^+$.

For $X(N_2H^+)$, we assume for 4A and 4B the value of 6.0×10^{-11} derived by B95 at 4A by comparing the observed column density of N$_2$H$^+$ with that suggested for H$_2$ by continuum observations of dust. This value is relatively low compared to mean values found in other cloud cores; Womack et al. (1992) and Benson et al. (1998) found mean values of $X(N_2H^+)$ of 4×10^{-10} and 7×10^{-10}, respectively, from various samples (see also Ungerechts et al. 1997). However, the sample of Womack et al. (1992) contains several cases in which $X(N_2H^+)$ is as low as or lower than 6.0×10^{-11}, e.g., ρ Oph and W49. Assuming a "canonical" CO abundance of 1×10^{-4}, B95 also derived a value for $X(N_2H^+)$ of 6.0×10^{-10}, more similar to the mean values of other cloud cores, by comparing column densities of N$_2$H$^+$ with that of H$_2$ suggested by C^{18}O and C^{17}O data. B95 suggested that this disparity could be reconciled if CO (and other molecules) in the nonoutflowing gas of IRAS 4 were depleted relative to dust by factors of 10–20 but maintained abundances relative to each other that were similar to those seen elsewhere.

Using equation (8) and the above assumptions, the M_{gas} of 4A and 4B are 0.73 and 0.41 $M_\odot$, respectively. As a comparison, recent SCUBA observations of continuum emission from dust around 4A and 4B by Sandell & Knee (2001) yield circumstellar mass estimates of 2.0–4.0 $M_\odot$ and 0.65–1.3 $M_\odot$, following their analysis but assuming a distance to NGC 1333 of 350 pc and a range of T_K of 20–40 K. (In their analysis, Sandell & Knee 2001 assumed $T_K = 25$ K and a 220 pc distance to derive masses.) The SCUBA-based masses are somewhat larger than ours, possibly as a result of their greater sensitivity to larger scale emission from lower density material.

Another comparison of mass is provided by virial masses of the nonoutflowing dense gas surrounding 4A and 4B. These can be calculated from the respective mean values of ΔV and apparent sizes as

$$M_{vir} = 210\left(\frac{R}{pc}\right)\left(\frac{\Delta V}{km\ s^{-1}}\right)^2 M_\odot , \qquad (9)$$

for a uniform, self-gravitating sphere (e.g., see Larson 1981). Using the mean values of ΔV listed in Table 4 and the values of R of 0.022 pc for 4A and 0.0093 pc for 4B (obtained from the extents of the integrated emission shown in Fig. 1*f*) in equation (9), virial masses of 1.1 and 0.48 $M_\odot$

are found for the nonoutflowing dense gas around 4A and 4B, respectively, values quite similar to those determined above from the derived column densities. [Alternatively, values of $X(N_2H^+)$ of 4.0×10^{-11} and 5.1×10^{-11}, similar to that found by B95 for 4A, can be found for 4A and 4B, respectively, by inverting eq. (8) and assuming $M_{vir} = M_{gas}$.]

4.3.2. Rotation

Figures 7*b* and 7*e* show the distributions of V_{LSR} with position around 4A and 4B, respectively, obtained from hyperfine structure fitting. Systematic variations with position of the central velocity, V_{LSR}, of the symmetric profiles of an optically thin line can suggest velocity gradients in the gas. If a gradient is found symmetrically about an average velocity and position, it may be caused by rotational motions of the gas.

As listed in Table 5, the mean V_{LSR} values of the nonoutflowing dense gas associated with 4A and 4B are 6.95 and 6.98 km s^{-1}, respectively, each within the mean fitting uncertainty of the other (0.032 km s^{-1}). If these mean velocities of this dense gas are representative of the radial velocities of the 4A and 4B objects themselves, the 4A and 4B objects are not moving relative to each other significantly along the line of sight, as might be expected if 4A and 4B were revolving about each other. (However, a V_{LSR} difference of 0.28 km s^{-1} is found between 4A and 4B from modeling their respective associated inverse P Cygni profiles; see § 4.2.1 and Table 3.) The average V_{LSR} obtained from the nonoutflowing dense gas around both objects is 6.96 km s^{-1}, which we take as the systemic velocity of IRAS 4.

Near 4A, the rms variation of V_{LSR} is more than half the mean ΔV, i.e., 0.36 km s^{-1} versus 0.25 km s^{-1}, suggesting that the variations of V_{LSR} around 4A are significant. Furthermore, the positional distribution of V_{LSR} in the nonoutflowing dense gas about 4A shows systematic, symmetrical variations that may be due to rotation. To first order, the southeastern half of this gas around 4A is blueshifted (relative to the mean) by ~ 0.25–0.5 km s^{-1}, and the northwestern half is redshifted by ~ 0.0–0.5 km s^{-1}, variations that could arise if this gas were rotating about 4A on an axis at a P.A. of $\sim 45°$. (Such an axis would be collinear with the "cavity" containing 4A and 4A'.) Rotating dense gas, however, cannot account for all variations of V_{LSR} about 4A. For example, two pockets to the north by northwest and one to the south by southwest have relative velocities in directions opposite to those expected from rotation at their locations. Given that the south by southwest pocket is unusually redshifted and that it lies in the same direction of the blue 4A outflow lobe (see § 4.2.2), the pocket may be a local distortion of a rotational velocity field due to selective clearing of N$_2$H$^+$ at blueshifted velocities by the outflow in

that direction. A similar explanation may account for the unusually blueshifted pockets in the same direction as the red outflow lobe. (The interpretation of velocity variations as caused by rotation is not unique, and the velocity distribution also could be due to bulk infall or outflow motions of gas on either side of 4A.)

Near 4B, the characteristics of V_{LSR} are much different from those seen around 4A. The rms variation of V_{LSR} is less than half the mean ΔV, i.e., 0.096 km s^{-1} versus 0.25 km s^{-1}, and only $\sim 25\%$ that of the nonoutflowing dense gas around 4A, suggesting that the variations of V_{LSR} are not significant. In addition, no systematic variation of V_{LSR} is seen with position, and hence no suggestion of rotation (and infall or outflow), at least from the N$_2$H$^+$ 1–0 line. The difference in rotational properties between the nonoutflowing dense gas surrounding 4A and 4B is striking in the context of binary formation. Since 4A is a known binary of 1″ (or 350 AU) separation but 4B has not been confirmed to be a multiple, the relatively large rotation of the nonoutflowing dense gas about 4A suggests that binaries may form preferentially in cores of relatively high intrinsic angular momentum but single stars form preferentially in cores of relatively low intrinsic angular momentum. (However, 4B may be yet a binary system, albeit with a much smaller separation than that of 4A and 4A′; see § 4.2.2.)

4.3.3. Turbulent Motions

NGC 1333 is located in the western Perseus molecular cloud, a region where a large number of stars are forming in close proximity from gas that is fairly turbulent, judging from the observed line widths. For example, IRAS 4A and 4B have among the largest N$_2$H$^+$ 1–0 line widths, 1.32 and 1.04 km s^{-1}, respectively, of the 47 Class 0 or Class I objects within 400 pc sampled by M97. As the thermal FWHM of N$_2$H$^+$ is 0.247 km s^{-1} if $T_K = 40$ K (i.e., the maximum of the T_K range derived by B95 for the nonoutflowing gas), the broad lines seen by M97 in IRAS 4 suggest the presence of substantial turbulent motions in the dense gas on scales of 0.05 pc (i.e., the 27″ IRAM 30 m telescope beam FWHM at 93.17 GHz at 350 pc).

The PdBI data described here probe physical scales much smaller than those of single-dish observations, e.g., the synthesized beam FWHM is only 0.0055 × 0.0064 pc at 350 pc. Figures 7c and 7f show the distributions of the N$_2$H$^+$ 1–0 line width near 4A and 4B, respectively, i.e., values of ΔV obtained from hyperfine structure fitting. Table 5 lists the beam-averaged mean, rms, maximum, and minimum values of ΔV found for nonoutflowing dense gas around 4A or 4B. From these data, a dramatic reduction in N$_2$H$^+$ line width is seen, relative to the single-dish data. For example, maximum beam-averaged values of ΔV around both objects are less than 0.84 km s^{-1}, and the mean beam-averaged values of ΔV are both only ~ 0.50 km s^{-1}, much less than seen in single-dish data.

At first glance, it is conceivable that the larger ΔV in single-dish observations could originate from the unresolved combination of intrinsically narrow lines with potentially wide variations of central line velocity in the dense gas (e.g., from rotation). However, the rms values of V_{LSR} and the mean values of ΔV are too small to support this possibility. Instead, the overall reduction of line width with scale in IRAS 4 may be a manifestation of the line width–size relation, as observed in many molecular clouds (e.g., see

McKee 1999 and references therein), and the interferometer data are probing the smallest scales of this relation. At these scales, the nonthermal component of the line width is predicted to be comparable in magnitude to the thermal component, possibly as a result of dissipation of turbulence (Vázquez-Semadeni et al. 2000) or the cutoff of MHD wave propagation (Nakano 1998; Myers 1998) at small scales.

A similar but less dramatic reduction of line width with scale was noted for eight "quiescent cores" in the Serpens NW cluster region by Williams & Myers (2000), which is presumed to be at a similar distance to NGC 1333 (i.e., 310 pc; de Lara, Chavarria-K, & Lopez-Molina 1991). In Serpens NW, the mean width ratio for lines observed between 10″ and 50″ resolution over all eight cores was 0.59, whereas the mean width ratio for lines observed between ~ 4″ and 27″ over 4A and 4B is 0.43, using the observations of M98 and the mean values of ΔV in Table 5. Interestingly, the eight cores found by Williams & Myers (2000) have typical sizes of ~ 5000 AU, line widths of ~ 0.5 km s^{-1}, and infall speeds of ~ 0.5 km s^{-1}, values all similar to those of the nonoutflowing dense gas around 4A and 4B (assuming that the infall speeds found in § 4.2.1 from H$_2$CO apply to the N$_2$H$^+$ gas).

Despite the overall relative reduction in line width with scale seen here, the high spatial resolution of these observations reveals significant variations in ΔV in the nonoutflowing dense gas around both objects (see Figs. 7c and 7f), and a common narrow width of ~ 0.5 km s^{-1} cannot describe the line emission. Figure 8 shows histograms of the distributions of ΔV as fractions of the total number of beam-averaged pixels around 4A (54 pixels) or 4B (12 pixels) in 0.15 km s^{-1} bins. Both have ranges of ΔV between 0.23 and 0.83 km s^{-1}, with substantial fractions (15%–30%) near 0.25 km s^{-1}, the thermal line width at 40 K, indicating the presence of very nonturbulent gas around each object. (Minimum beam-averaged ΔV values of 0.21 km s^{-1} near 4A and 0.16 km s^{-1} near 4B are found, located north of 4A and 4B, or at the peripheries of the dense gas.) Of the remainder, the distribution for 4A has peaks at 0.38 and 0.68 km s^{-1}, but that of 4B has only a peak at 0.23 km s^{-1}. For 4A, lines of the first peak are located generally to the northwest and lines of the second peak are located generally to the southeast, although the populations are mixed. For 4B, the lines broaden systematically from north to south across its dense gas.

The condensations from which 4A and 4B formed may be plausibly assumed to have had nearly uniform initial velocity dispersions, as is seen in many starless dense cores (see Goodman et al. 1998; P. Caselli et al. 2001, in preparation). The star formation process from that time until the present likely increased the velocity dispersion by differing amounts throughout each condensation, mainly as a result of modest outflow-core interaction or heating from the protostars, but very likely did not decrease the dispersion anywhere. Every independent measurement of line width in the gas around each object then gives an upper limit on the initial velocity dispersion of the original condensation. The typical upper limit comes from the mean present-day line width, ~ 0.5 km s^{-1} in both 4A and 4B, and the most constraining upper limit comes from the narrowest present-day line width, ~ 0.2 km s^{-1} in the gas around both 4A and 4B. These new limits indicate that the initial level of turbulence in star-forming condensations may be very low, even in regions of clustered star formation. For example, if $T_K = 20$ K (the low
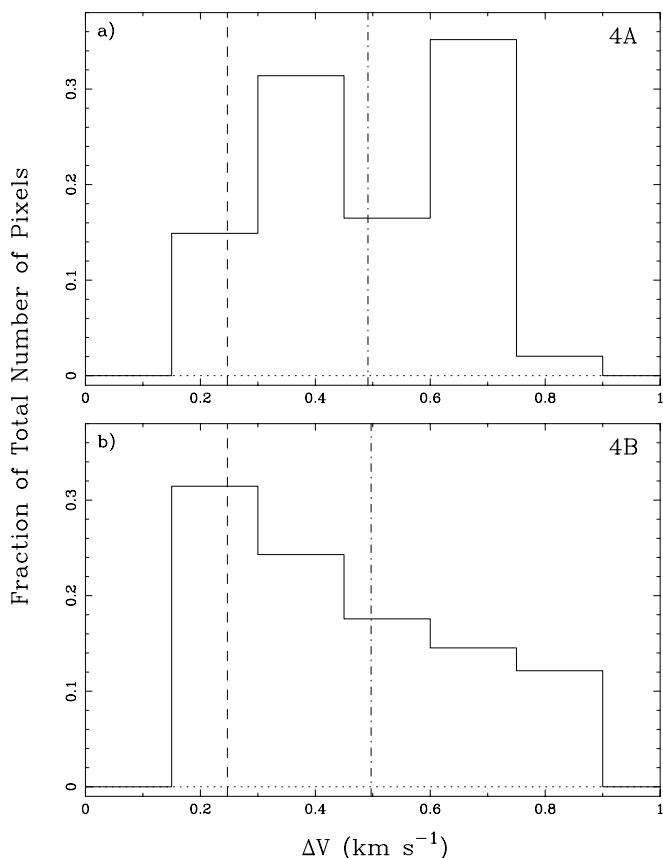
FIG. 8.—Distribution of ΔV from N_2H^+ 1–0 emission around (*a*) 4A and (*b*) 4B in 0.15 km s^{-1} wide bins as fractions of the total number of nonblanked pixels, i.e., 54 pixels for 4A and 12 pixels for 4B. (The criterion for blanking is the same as for Fig. 7.) Values of ΔV are obtained by deconvolving the measured values by the 0.16 km s^{-1} velocity resolution of the PdBI correlator. The dashed line indicates the FWHM expected from the N_2H^+ 1–0 line from thermal broadening only at $T_K = 40$ K, the maximum T_K estimated for the nonoutflowing gas around 4A by B95. The dot-dashed line indicates the mean ΔV measured from spectra around each protostellar object.

end of T_K from B95) and ΔV(observed) = 0.225 km s^{-1} (the lowest ΔV bin in Fig. 8), then ΔV(thermal) = 0.18 km s^{-1} for N_2H^+ and ΔV(nonthermal) = 0.135 km s^{-1}, as ΔV(nonthermal) = $[\Delta V^2(\text{observed}) - \Delta V^2(\text{thermal})]^{0.5}$.

If the velocity dispersion has evolved from its initial state though the injection of energy, line widths arguably should be largest at positions closest to possible sources of energy, and there is indeed some evidence for this in the dense gas around both objects. For example, there appears to be some spatial correspondence between large values of ΔV and the blueshifted outflow features (as traced by H_2CO) south of both 4A and 4B. However, the situation is not so clear cut, and evidence to the contrary is also found. For example, the narrowest lines in the nonoutflowing dense gas around 4A and 4B are found actually near the respective red outflow features north of each object. Moreover, large line widths are found across the southeastern half of the 4A dense gas, not just at positions near the blue outflow lobe. Given the factor of ~ 10–20 difference between the spectral width of the H_2CO wings and the width of the N_2H^+ line even at positions of large ΔV, whatever coupling does exist between the dense outflowing gas and N_2H^+ appears to be very inefficient.

The weak coupling between the fast outflow and the non-outflowing gas may be a consequence of their difference in speed, with greater coupling expected when the flow speed is more comparable to the velocity dispersion of its environment. On the other hand, possibly the N_2H^+ is depleted more rapidly than it can be accelerated to speeds similar to the outflow. (The contrast of widths cannot be ascribed to the outflow gas being less dense than the nonoutflowing gas, as both transitions probe gas at $n \approx 10^5$–10^6 cm^{-3}.) Similar contrasts in line width have been found toward other very young objects, but the proximity of outflow gas to the nonoutflowing gas is not so clearly defined in single-dish observations. For example, the survey of M97 contains several examples with outflow wings in H_2CO and CS, but not in N_2H^+, on 0.02–0.05 pc scales, toward sources such as L483, S68N, or L1157 (and, of course, 4A and 4B). The PdBI data here show that emission from both outflowing and nonoutflowing gas around 4A and 4B can be spatially coincident on scales of only ~ 0.006 pc.

5. SUMMARY AND CONCLUSIONS

Millimeter interferometer observations are presented of NGC 1333 IRAS 4, a group of highly embedded protostellar objects in the Perseus star-forming complex. Millimeter continuum data and line data allow the immediate dense gas and dust environments of its protostellar objects to be characterized simultaneously at high spatial resolution. The major results found from these observations include the following:

1. Inverse P Cygni profiles of H_2CO 3_{12}–2_{11} that show redshifted absorption and blueshifted emission have been detected toward 4A and 4B. Inverse P Cygni profiles of CS 3–2 and N_2H^+ 1–0 also have been detected toward 4A. These profiles provide the least ambiguous evidence for infalling gas motions associated with low-mass young stellar objects. The depths of the absorption in the H_2CO line are equal to the $\lambda = 1.3$ mm continuum intensities of the protostars along the same lines of sight. Modeling the H_2CO profiles with a "two-layer" radiative transfer code, infall velocities toward 4A and 4B of 0.68 and 0.47 km s^{-1} are estimated, respectively. From these, masses of 0.71 and 0.23 $M_\odot$ and accretion rates, $\dot{M}_{in}$, of 1.1×10^{-4} and 3.7×10^{-5} $M_\odot$ yr^{-1} for 4A and 4B are estimated, respectively, given assumptions about r_{in} and n. Accretion timescales for both objects are similar, with $t_{acc} = \dot{M}/M$ of 6500 and 6200 yr for 4A and 4B, respectively.

2. Outflowing gas from both 4A and 4B is detected from bright wing emission of H_2CO 3_{12}–2_{11} and CS 3–2. The outflows from each source differ, in that only the southern blue lobe from the extended outflow from 4A is detected but four to five compact features from 4B are detected. For 4A, the velocity structure of the emission suggests that the H_2CO is tracing outflow cavity walls. The orientation of the cavity walls suggests that the outflow has precessed from orientations evident at larger scales, possibly as a result of the binarity of 4A. For 4B, the multipolar structure could be also from cavity walls of an outflow that is more compact than that from 4A. However, the complex structure may originate from several juxtaposed lobes from a multiple object.

3. Nonoutflowing dense gas surrounding 4A and 4B individually is detected from N_2H^+ 1–0 emission. With assumptions, we determine mean column densities of

2.4×10^{12} and 3.9×10^{12} cm^{-2}, respectively. Furthermore, masses of this gas are estimated to be 0.73 and 0.41 $M_\odot$, respectively, comparable to other estimates of circumstellar mass derived from submillimeter dust emission and the virial theorem. The variations of V_{LSR} around each object suggest that the nonoutflowing dense gas about 4A is rotating, but the data do not suggest similar motions about 4B.

4. The widths of the N$_2$H$^+$ 1–0 line in the nonoutflowing dense gas around both 4A and 4B are smaller by factors of 2–3 on average than those observed in single-dish data, as a result of the reduction of turbulent motions on smaller physical size scales. The data reveal a new, low upper bound to the initial velocity dispersion in the protostellar core from which IRAS 4 formed. For example, some regions around each object ($\sim$15%–30% of the projected surface areas of line emission) exhibit lines with very narrow widths, e.g., $\sim$0.2 km s^{-1}. Such narrow line widths are consistent with the incoherent motions of the gas having a nonthermal component of a magnitude comparable to that of thermal broadening at expected gas temperatures and may represent the initial state of the core gas prior to the formation of the protostars or their outflows. The lines show consider-

able variation of width, however, even on the small scales probed. Coupling between outflow and the nonoutflowing dense gas, which could inject turbulent energy into any initially nonturbulent gas, appears highly inefficient, as line widths from H$_2$CO and N$_2$H$^+$ can differ by factors of 10–20 on scales of only 0.006 pc.

APPENDIX

HIGH-RESOLUTION CONTINUUM OBSERVATIONS OF NGC 1333 IRAS 4

Table 2 lists the flux densities, peak intensities, and deconvolved sizes of each source, derived from fitting single-component two-dimensional Gaussians to observations of each source individually at each wavelength with the AIPS task IMFIT. (Positions are also defined by these fits, e.g., those shown in Fig. 1 are those of the peak continuum intensities at $\lambda = 1.3$ mm from Gaussian fitting.) Flux density uncertainties are comprised of those derived from the fits, an assumed 15% uncertainty in the absolute calibration at each wavelength, and an estimated 10% measurement uncertainty. Values in Table 2 for 4B' at $\lambda = 1.3$ mm are particularly uncertain as a result of its location at the mosaic edge (see Fig. 1a), although the peak position obtained from the fit agrees quite well with those from other wavelengths.

Figure 9 shows the millimeter wavelength SEDs of each IRAS 4 object from our continuum data. In addition, Figure 9 shows data obtained at $\lambda = 800$ μm by Lay et al. (1995) from the JCMT-CSO Interferometer, at $\lambda = 1.3$ and 3.6 cm by Mundy et al. (1993) at the VLA, and at $\lambda = 3.6$ and 6.0 cm by Rodríguez et al. (1999) at the VLA. At all wavelengths, 4A is brighter than 4B, which is in turn brighter than 4B'. The SEDs of Figure 9 are reasonably well fitted by straight lines of similar slopes, i.e., $\alpha_1 = -2.7 \pm 0.05$ for 4A, -2.9 ± 0.14 for 4B, and -2.6 ± 0.23 for 4B', using linear least-squares fitting over the range 1.3 mm $< \lambda <$ 1.3 cm. For 4A and 4B, only our data at $\lambda = 1.3$ cm were included for the fit, as they are similar (i.e., within errors) to those found by Mundy et al. (1993) at the same wavelength. For 4B', the linear fit included the flux density at $\lambda = 1.3$ mm, although this measurement is particularly uncertain, and excluded our upper limit at $\lambda = 1.3$ cm.

The similar slopes reveal that continuum emission for the IRAS 4 objects at $\lambda < 1.3$ cm is dominated by thermal emission from dust grains surrounding each source. Given the deconvolved sizes of the emission, the warm dust being traced is likely situated within accretion disks or the inner radii of envelopes around each source. If the dust emission is optically thin (and we assume that the same region is probed) at all wavelengths, the slope, α, can be used to estimate the indices of the mass opacity of dust, i.e., β. As $-\alpha = \beta + 2$ in the Rayleigh-Jeans limit, dust opacity indices of 0.7 ± 0.05 for 4A, 0.9 ± 0.14 for 4B, and 0.6 ± 0.25 for 4B' are found from our α_1, each consistent with a common value of $\beta \approx 0.75$ and significantly less than the $\beta = 2$ value assumed typically for dust in the ISM. These values are similar to the $\beta \approx 1$ values inferred for dust around many other young stellar objects, a decrease in β possibly due to growth or composition changes of the dust (Beckwith & Sargent 1991).

The submillimeter wavelength data of Lay et al. (1995), not included in the linear fits shown in Figure 9, deviate from the derived fits because they were obtained at a resolution of $\sim$1″, and much of the emission from dust in the inner radii of envelopes may have been resolved out in those data. The centimeter wavelength data of Rodríguez et al. (1999), also not included in the linear fits, deviate dramatically from the lines fitted solely to the data at $\lambda \leq 1.3$ cm, suggesting that free-free emission becomes increasingly dominant in the SEDs of these sources at long wavelengths. Extrapolating these data to shorter wavelengths, the contribution of this emission to the respective flux densities is small, i.e., less than 20% at $\lambda = 1.3$ cm and less than 5% at $\lambda = 6.9$ mm for both 4A or 4B.

Departures of individual flux densities at millimeter wavelengths from the linear fits are seen least in the fit to the 4B SED, whose reduced $\chi^2 = 1.6$, but are seen more for the fits to the 4A SED (reduced $\chi^2 = 7.9$) and 4B' SED (reduced $\chi^2 = 9.5$). The latter large values of reduced χ^2 may be due to underestimates of the absolute flux calibration uncertainties.

At specific wavelengths, the largest departures from the linear fits are the positive ones found at $\lambda = 3.2$ mm for all three objects. The object 3C 84 was also observed during all tracks as IRAS 4, but a similar positive departure of its flux density at
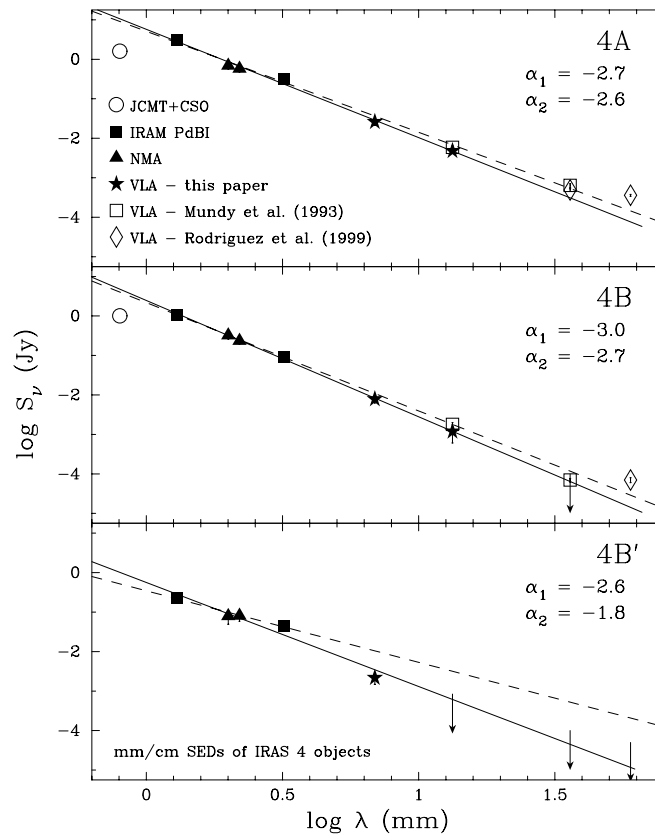
Fig. 9.—SEDs of 4A, 4B, and 4B' objects from interferometer continuum observations between $\lambda = 800\ \mu m$ and 6 cm. Filled squares, filled triangles, and filled stars show data obtained, respectively, from the IRAM PdBI, the NRO NMA, and the NRAO VLA for this paper. The open circles show data at $\lambda = 800\ \mu m$ from the JCMT-CSO Interferometer by Lay et al. (1995) for 4A and 4B. Open squares show data at $\lambda = 1.3$ and 3.6 cm from Mundy et al. (1993), and open diamonds show data at $\lambda = 3.6$ and 6.0 cm by Rodriguez et al. (1999) for 4A and 4B all from the VLA. Downward-pointing arrows indicate 3 σ upper limits. Error bars are 1 σ (see text and Table 2). Solid lines indicate lines of slope α_1 resulting from linear least-squares fits to our flux densities of each object at 1.3 mm $< \lambda <$ 1.3 cm. Dashed lines indicate lines of slope α_2 resulting from similar fitting but using only our data at $1.3 < \lambda < 3.2$ mm.

$\lambda = 3.2$ from a linear fit is not seen. This consistency suggests that the deviations in the IRAS 4 SEDs from their fits at this wavelength may be real, and the slopes of the IRAS 4 SEDs at $\lambda \leq 3.2$ mm may be shallower than those found in earlier fits. Dust emission at $\lambda > 3.2$ mm may be declining at a steeper overall slope, possibly because the cooler, outer layers of the IRAS 4 envelopes are resolved out at our high resolutions or have lower optical depths than the inner regions.

Slightly shallower slopes of the linear fits are found for the 4A and 4B SEDs if our VLA data are additionally excluded from the fits, i.e., $\alpha_2 = -2.6 \pm 0.29$ and -2.7 ± 0.30, respectively, but these do not differ significantly from slopes obtained with the VLA data included. One slope that does differ significantly is that of 4B', namely, $\alpha_2 = -1.8 \pm 0.39$. The slopes of all three SEDs change only slightly if the NMA data are also excluded. Unlike for 4A and 4B, both α_1 and α_2 for 4B' are significantly more than the values of -3.8 or -3.9 derived by Choi (2001) from interferometer continuum data at $\lambda = 3.4$ and 2.7 mm. Values of β derived from our slopes suggest that 4B' could have dust with significantly different opacity than 4A and 4B, possibly from a population of larger dust grains. Alternatively, the dust may be optically thick. Given the dimness of 4B' relative to 4A or 4B, more sensitive data than those shown here (especially at $\lambda = 1.3$ and 6.9 mm) are needed to properly evaluate either possibility.

REFERENCES

Adelson, L. M., & Leung, C. M. 1988, MNRAS, 235, 349
Akeson, R. L., Carlstrom, J. E., Phillips, J. A., & Woody, D. P. 1996, ApJ, 456, L45
André, P., Ward-Thompson, D., & Barsony, M. 1993, ApJ, 406, 122
Arons, J., & Max, C. E. 1975, ApJ, 196, L77
Bachiller, R. 1996, ARA&A, 34, 111
Bachiller, R., & Pérez-Gutiérrez, M. 1997, ApJ, 487, L93
Beckwith, S. V. W., & Sargent, A. I. 1991, ApJ, 381, 250
Benson, P. J., Caselli, P., & Myers, P. C. 1998, ApJ, 506, 743
Bergin, E. A., & Langer, W. D. 1997, ApJ, 486, 316
Bergin, E. A., Neufeld, D. A., & Melnick, G. J. 1998, ApJ, 499, 777
Blake, G. A., Sandell, G., van Dishoeck, E. F., Groesbeck, T. D., Mundy, L. G., & Aspin, C. 1995, ApJ, 441, 689 (B95)
Bontemps, S., André, P., Terebey, S., & Cabrit, S. 1996, A&A, 311, 858
Cabrit, S., & Bertout, C. 1986, ApJ, 307, 313
Caselli, P., Myers, P. C., & Thaddeus, P. 1995, ApJ, 455, L77
Cernis, K. 1990, Ap&SS, 166, 315

Choi, M. 2001, ApJ, 553, 219
Choi, M., Panis, J.-F., & Evans, N. J., II 1999, ApJS, 122, 519
Crutcher, R. 1999, ApJ, 520, 706
de Lara, E., Chavarria-K, C., & Lopez-Molina, G. 1991, A&A, 243, 139
Di Francesco, J., Evans, N. J., II, Harvey, P. M., Mundy, L. G., Guilloteau, S., & Chandler, C. J. 1997, ApJ, 482, 433
Evans, N. J., II 1999, ARA&A, 37, 311
Goodman, A. A., Barranco, J. A., Wilner, D. J., & Heyer, M. H. 1998, ApJ, 504, 223
Green, S. 1991, ApJS, 76, 979
Green, S., Montgomery, J. A., Jr., & Thaddeus, P. 1974, ApJ, 193, L89
Gregersen, E., Evans, N. J., II, Zhou, S., & Choi, M. 1997, ApJ, 484, 256
Herbig, G. H., & Jones, B. F. 1983, AJ, 88, 1040
Ho, P. T. P., & Young, L. M. 1996, ApJ, 472, 742
Jennings, R. E., Cameron, D. H. M., Cudlip, W., & Hirst, C. J. 1987, MNRAS, 226, 461
Keto, E., Ho, P. T. P., & Haschick, A. D. 1987, ApJ, 318, 712

Keto, E., Ho, P. T. P., & Haschick, A. D. 1988, ApJ, 324, 920
Knee, L. B. G., & Sandell, G. 2000, A&A, 361, 671
Lada, E. A., Strom, K. M., & Myers, P. C. 1993, in Protostars & Planets III, ed. E. H. Levy, J. I. Lunine, & M. S. Matthews (Tucson: Univ. Arizona Press), 245
Larson, R. B. 1981, MNRAS, 194, 809
Lay, O. P., Carlstrom, J. E., & Hills, R. E. 1995, ApJ, 452, L73
Lee, C. W., Myers, P. C., & Tafalla, M. 2001, ApJS, 136, 703
Lefloch, B., Castets, A., Cernicharo, J., Langer, W. D., & Zylka, R. 1998, A&A, 334, 269
Leung, C. M., & Brown, R. L. 1977, ApJ, 214, L73
Looney, L. W., Mundy, L. G., & Welch, W. J. 2000, ApJ, 529, 477
Mardones, D. 1998, Ph.D. thesis, Harvard Univ. (M98)
Mardones, D., Myers, P. C., Tafalla, M., Bachiller, R., Wilner, D. J., & Garay, G. 2001, ApJ, submitted
Mardones, D., Myers, P. C., Tafalla, M., Wilner, D. J., Bachiller, R., & Garay, G. 1997, ApJ, 489, 719 (M97)
Mathieu, R. D. 1994, ARA&A, 32, 465
McKee, C. F. 1999, in The Origin of Stars and Planetary Systems, ed. C. J. Lada & N. D. Kylafis (Dordrecht: Kluwer), 29
Mundy, L. G., McMullin, J. P., Grossman, A. W., & Sandell, G. 1993, Icarus, 106, 11
Myers, P. C. 1998, ApJ, 496, L109
Myers, P. C., Mardones, D., Tafalla, M., Williams, J. P., & Wilner, D. J. 1996, ApJ, 465, L133
Nakano, T. 1998, ApJ, 494, 587

Ohashi, N., Hayashi, M., Ho, P. T. P., Momose, M., Tamura, M., Hirano, N., & Sargent, A. I. 1997, ApJ, 488, 317
Plambeck, R. L., & Engargiola, G. 1999, in ASP Conf. Ser. 217, Imaging at Radio through Submillimeter Wavelengths, ed. J. G. Mangum & S. J. E. Radford (San Francisco: ASP), 354
Rodriguez, L. F., Anglada, G., & Curiel, S. 1999, ApJS, 125, 427
Sandell, G., Aspin, C., Duncan, W. D., Russell, A. P. G., & Robson, E. I. 1991, ApJ, 376, L17
Sandell, G., & Knee, L. B. G. 2001, ApJ, 546, L49
Smith, K. W., Bonnell, I. A., Emerson, J. P., & Jenness, T. 2000, MNRAS, 319, 991
Ungerechts, H., Bergin, E. A., Goldsmith, P. F., Irvine, W. M., Schloerb, F. P., & Snell, R. L. 1997, ApJ, 482, 245
Vázquez-Semadeni, E., Ostriker, E. C., Passot, T., Gammie, C. F., & Stone, J. M. 2000, in Protostars and Planets IV, ed. V. Mannings, A. P. Boss, & S. S. Russell (Tucson: Univ. Arizona Press), 3
Welch, W. J., Dreher, J. W., Jackson, J. M., Terebey, S., & Vogel, S. N. 1987, Science, 238, 1550
Williams, J. P., & Myers, P. C. 2000, ApJ, 537, 891
Williams, J. P., Myers, P. C., Wilner, D. J., & Di Francesco, J. 1999, ApJ, 513, L61
Womack, M., Ziurys, L. M., & Wyckoff, S. 1992, ApJ, 387, 417
Zhang, Q., & Ho, P. T. P. 1997, ApJ, 488, 241
Zhang, Q., Ho, P. T. P., & Ohashi, N. 1998, ApJ, 494, 636
Zhou, S., Evans, N. J., II, Koempe, C., & Walmsley, C. M. 1993, ApJ, 404, 232